CopERnIcus climate change Service Evolution

D1.4 Observation operator methodology ready for implementation

Due date of deliverable	31st December 2025
Submission date	11th December 2025
File Name	CERISE-D1-4-V1.0
Work Package /Task	WP1 Task 1.4
Organisation Responsible of Deliverable	Estellus
Author name(s)	Iris de Gelis, Jostein Blyverket, Filipe Aires, Catherine Prigent, Asmund Bakketun, Cyril Palerme, Harald Schyberg, Ilaria Clemenzi, Jude Musuuza, David Gustafsson
Revision number	V1.0
Status	ISSUED
Dissemination Level	PUBLIC

Funded by the European Union

The CERISE project (grant agreement No 101082139) is funded by the European Union.
Views and opinions expressed are however those of the author(s) only and do not necessarily reflect those of the European Union or the Commission. Neither the European Union nor the granting authority can be held responsible for them.

1. Executive Summary

This report describes the development of ML-based observation operators for low frequency passive microwave satellite instruments to enable the direct assimilation of L1 brightness temperatures over land (both snow covered and snow free). A variety of ML algorithms are explored including multi-layer perceptrons and graph neural networks amongst others. The models are trained using features from the ERA5 reanalysis, surface water climatology, offline SURFEX model simulations and observations from the SMOS, SMAP and AMSR2 instruments as targets.

A thorough information content analysis is first performed to choose which model variables are most strongly correlated with the observed brightness temperatures or microwave emissivities. Then, using the chosen model features the ML observation operators are trained using historical data and validated using independent data not used in the training.

The performance of the models is assessed by evaluating the predicted outputs against the targets using various statistical metrics. In addition, the ML observation operators are compared against alternative models such as climatologies of the outputs and physics-based models.

Initial results show improved performance over snow-covered regions for the global emissivity ML-based model compared to existing climatologies. Over snow-free areas at higher frequencies the ML-based model struggles to outperform the climatologies due to smaller spatio-temporal variations in the emissivities and a lack of inter-annually varying predictors. At lower frequencies the ML-based model performs better where variations in emissivity are more strongly linked to soil moisture variations.

For the models trained over the regional Scandinavian domain the performance varies depending on the time of year (related to snow accumulation and melting periods), location (with worse performance in complex terrain) and the choice of ML algorithm. The best performance is with the dynamic graph neural network but this has the downside that it is computationally expensive to train, so the most promising algorithm is the static graph neural network. The performance of this model compares favourably to the physically based CMEM which is promising for future data assimilation experiments.

Table of Contents

2. Introduction

This deliverable is a report to document the methodologies used to develop the machine-learning (ML) based observation operators for use both in global (IFS) and regional (HARMONIE_AROME) systems in CERISE WPs 2 & 4. The training, validation, testing and evaluation of the operators will be described, as well as the observations and microwave frequencies they are targeted at, and next steps for testing in the assimilation systems will be outlined.

2.1. Background

The scope of CERISE is to enhance the quality of the C3S reanalysis and seasonal forecast portfolio, with a focus on land-atmosphere coupling.

It will support the evolution of C3S, over the project's 4 year timescale and beyond, by improving the C3S climate reanalysis and the seasonal prediction systems and products towards enhanced integrity and coherence of the C3S Earth system Essential Climate Variables.

CERISE will develop new and innovative ensemble-based coupled land-atmosphere data assimilation approaches and land surface initialisation techniques to pave the way for the next generations of the C3S reanalysis and seasonal prediction systems.

These developments will be combined with innovative work on observation operator developments integrating Artificial Intelligence (AI) to ensure optimal data fusion fully integrated in coupled assimilation systems. They will drastically enhance the exploitation of past, current, and future Earth system observations over land surfaces, including from the Copernicus Sentinels and from the European Space Agency (ESA) Earth Explorer missions, moving towards an all-sky and all-surface approach. For example, land observations can simultaneously improve the representation and prediction of land and atmosphere and provide additional benefits through the coupling feedback mechanisms. Using an ensemble-based approach will improve uncertainty estimates over land and lowest atmospheric levels.

By improving coupled land-atmosphere assimilation methods, land surface evolution, and satellite data exploitation, R&I inputs from CERISE will improve the representation of long-term trends and regional extremes in the C3S reanalysis and seasonal prediction systems.

In addition, CERISE will provide the proof of concept to demonstrate the feasibility of the integration of the developed approaches in the core C3S (operational Service), with the delivery of reanalysis prototype datasets (demonstrated in pre-operational environment), and seasonal prediction demonstrator datasets (demonstrated in relevant environment).

CERISE will improve the quality and consistency of the C3S reanalysis systems and of the components of the seasonal prediction multi-system, directly addressing the evolving user needs for improved and more consistent C3S Earth system products.

2.2. Scope of this deliverable

2.2.1. Objectives of this deliverable

This deliverable documents the methodologies used to develop the ML-based observation operators to enable the direct assimilation of low frequency microwave level 1 radiances over land.

2.2.2. Work performed in this deliverable

In this deliverable the work outlined in WP1 T1.4 (Develop land surface observation operator for the low frequency passive MW (1.4-36GHz) to link MW radiances to multiple model variables simultaneously) is described and evaluated. The work is split into two main parts with one methodology designed for use in a global coupled data assimilation system described in section 3. A second methodology designed for use in a regional coupled data assimilation

system is described in section 4. The reason the work has been split in this way is because the two systems are sufficiently different in terms of configuration, climatology, domain covered and satellite data assimilated to require two separate observation operators to be developed. Conclusions and next steps are described in section 5.

2.2.3. Deviations and counter measures

No deviations have been encountered.

2.2.4. Reference Documents

[1] Project 101082139- CERISE-HORIZON-CL4-2021-SPACE-01 Grant Agreement

2.2.5. CERISE Project Partners:

ECMWF	European Centre for Medium-Range Weather Forecasts
Met Norway	Norwegian Meteorological Institute
SMHI	Swedish Meteorological and Hydrological Institute
MF	Météo-France
DWD	Deutscher Wetterdienst
CMCC	Euro-Mediterranean Center on Climate Change
BSC	Barcelona Supercomputing Centre
DMI	Danish Meteorological Institute
Estellus	Estellus
IPMA	Portuguese Institute for Sea and Atmosphere
NILU	Norwegian Institute for Air Research
MetO	Met Office

3. ML-based observation operator for use in a global coupled assimilation system

3.1. Scope of this deliverable

3.1.1. Objectives of this deliverable

The need for accurate microwave surface emissivity models for all Earth surfaces has long been recognized (English, 1999; Weng et al., 2001), for the retrieval of surface and atmospheric parameters from satellites, as well as for the assimilation of surface-sensitive satellite observations in Numerical Weather Prediction (NWP). However, assimilating surface-sensitive observations still remains far more difficult over continental surfaces than over the ocean, primarily due to their typically higher microwave emissivities, as well as complex spatial and temporal variability (Bormann et al., 2017). As a consequence, in NWP, a significant portion of the observations over continental surfaces is discarded, especially over snow-covered surfaces. Advancing 'all-surface' assimilation (Lawrence et al., 2019; Geer et al., 2022) is the next challenge in NWP developments, towards coupled land-ocean-atmosphere assimilation (de Rosnay et al., 2022), with expected improvements for atmosphere and surface characterization, and consequently forecasts.

Toward this goal, the objective of this deliverable is to develop land surface observation operators for the low frequency passive microwaves (1.4 - 36 GHz) to link microwave radiances to multiple model variables simultaneously. It will cover snow as well as snow-free surfaces at global scale.

3.1.2. Work performed in this deliverable

The work performed in this deliverable closely followed the Description of Action (WP1.4)

1. A large database of emissivities has been calculated directly from satellite measurements at the five frequencies of interest (1.4, 6, 10, 18 and 36GHz), by subtracting the atmospheric contribution and the surface temperature modulation from the observations. The emissivities are collocated with geophysical information describing the surface (snow, vegetation, humidity…), extracted preferably from ECMWF reanalysis.

2. The database has been analyzed to identify the relevant surface predictor that could explain the emissivities. This is an essential preliminary step for the model development phase. Snow and snow-free surfaces are treated separately.

3. Neural networks (NNs) have been trained to reproduce the emissivities from the relevant geophysical predictors. Multiple tests have been performed to reach an optimum solution.

4. The NN-based observation operator for land, and snow has been delivered to ECMWF for tests in the ECMWF system.

5. The simulated emissivities have been carefully evaluated, for the 5 frequencies, at a global scale and for all seasons.

3.2. Preparation of the training database

3.2.1. The satellite-derived emissivities

3.2.1.1. The calculation method

Microwave emissivities are directly calculated from satellite observations, removing the modulation by the surface temperature and the contribution from the atmosphere (gases and

clouds). It follows the methodology developed by Prigent et al. (1997), Karbou et al. (2008), Baordo and Geer (2016), or Munchak et al. (2020).

The methodology has already been described in detail. For each frequency and polarization, a simplified radiative transfer equation can be written as:

$$Tb = Tsurf \times emis \times \tau + T\downarrow atm \times (1 - emis) \times \tau + T\uparrow atm,$$

with emis the emissivity, Tb the satellite observed brightness temperature, Tsurf the temperature at the surface, T↓atm the downwelling atmospheric brightness temperature at the surface, T↑atm the upwelling atmospheric brightness temperature contribution, and τ the atmospheric transmission. This leads to:

$$emis = (Tb - T\uparrow atm - T\downarrow atm \times \tau) / (\tau \times (Tsurf - T\downarrow atm))$$

The calculation assumes that the surface temperature is the temperature of the emitting layer. If the radiation only emanates from the surface (i.e., the penetration depth or the sampling depth at that frequency is zero), the surface temperature is the actual surface “skin” temperature. However, emission from below the surface and volume scattering occur for a variety of surfaces, including snow and ice, with the penetration depth usually increasing with increasing wavelength. The above equations then imply an “effective” emissivity and an “effective” surface temperature, aggregated over the depth of penetration of the radiation within the sub-surface.

The ERA5 meteorological reanalysis provides hourly estimates of a large number of atmospheric and surface parameters (Hersbach et al., 2020). The ERA5 hourly surface skin temperature (Tskin) is selected for the emissivity calculation, spatially and temporally interpolated to the satellite observation location and time. In the above equations, t, T↑atm, T↓atm are estimated using a radiative transfer model (here Rosenkranz, 2017) and the atmospheric description from the ERA5 meteorological reanalyses. The cloud and rain liquid water effect in the atmospheric column has been taken into account, with the information provided by the time and space coincident ERA5 data, assuming Rayleigh-Jeans approximation. However, the cloud and rain are filtered in this study, for ERA5 total liquid water path above 0.05 kg/m2. Note that potential scattering by liquid and ice particles is neglected, with limited effect expected in the considered frequency range. Uncertainties in the emissivity calculations have been assessed for instance in Prigent et al. (1997) and Munchak et al. (2020).

3.2.1.2. The satellite data

The emissivities are systematically calculated at the swath level from AMSR2, SMAP, and SMOS observations, for all land surfaces and all ocean areas that are possibly sea ice covered. Calculations have been performed for all available satellite data, soon after their launch and up to 2020.

AMSR2 onboard the JAXA GCOM-W1 satellite measures at 6.925, 7.3, 10.65, 18.7, 23.8, 36.5, and 89.0 GHz, in both V and H polarizations, with an observing incidence angle of 55°, and with ground spatial resolutions ranging from 4 to 48 km depending on the channel frequency (JAXA, 2013). The AMSR2 Tbs are sourced from the JAXA data center. The level L1R product containing Tbs at the swath locations with original spatial resolutions is used (Maeda et al., 2016).

The SMAP mission (Entekhabi et al., 2010) provides 1.4 GHz (L-band) Tb at V and H polarizations at an incidence angle of 40° and with a spatial resolution of ~40 km. The SMAP data are obtained from Remote Sensing Systems (RSS). The L2C product provides Tbs resampled onto a fixed 0.25° Earth grid (Meissner et al., 2022). Different processing stages are available and the Tbs corresponding to the surface emission is used here, where all other Tb contributions are removed with the help of auxiliary data and radiative transfer modeling.

The SMAP sensor benefits from an advanced Radio Frequence Interference (RFI) detector, and RFI-affected Tb are not considered.

SMOS provides multi-angular and full-polarization observations at L-band (1.4 GHz) since 2009, using a Y shaped interferometric instrument, with a spatial resolution from 35 to 50 km depending on the incidence angle (Kerr et al., 2010). The SMOS data are collected from the Center Aval de Traitement des Données SMOS (CATDS). The L3C product includes V and H polarization Tbs, projected onto the ground and binned into 14 fixed angle classes of 5°, from 2.5 to 62.5° (Al Bitar et al., 2017). SMOS data affected by RFI are filtered out as much as possible (Uranga et al., 2022), using a threshold (0.4) on the flag provided by the CATDS.

3.2.2. The geophysical parameters

ERA5 reanalysis combines model outputs with multiple observations (in situ as well as satellites) into a globally complete and consistent data set, using physics laws (Hersbach et al., 2020). The data are projected onto a 0.25° regular grid in longitude and latitude. It is acquired through the Copernicus climate data store (https://cds.climate.copernicus.eu/cdsapp!/dataset/reanalysis-era5-single-levels?tab=overview).

The coincident hourly ERA5 parameters are collected, for each satellite swath data, possibly interpolated in space and time.

Some key additional information is not available from ERA5 and will be sourced externally, such as the Above Ground Biomass or the dynamic of the surface water extent. Note that the selected sources for these parameters are well established and broadly used by the community.

3.2.3. Practical consideration

Data are collected over one year. For the robustness of the parameterization and for practicality, the initial satellite-derived emissivities (at swath level) are projected onto a fixed grid of 12.5km and a 10-day compositing is performed by averaging for each cell (and angle bin for SMOS). This time compositing reduces the noise observed in the instantaneous emissivities and it is compatible with the monthly averaging often used in other studies (for each month, averaging over days 1-10, 11-20, and for the rest of the month). It is important to ensure that the database is thoroughly cleaned to create a reliable and robust forward model. Climatological emissivity records at 10-day resolution are computed based on the emissivity database for each instrument, from the averaging of all the estimated emissivities over the corresponding 10-day per year (per frequency, polarization, and possibly angle bin).

3.3. Parameterization methodology

3.3.1. Joint analysis of geophysical parameters and microwave emissivities

Before any attempt to parameterize the emissivities as a function of geophysical parameters, it is very important to carefully analyze the statistics of the training dataset and to analyze the relationship between the emissivities and the potential predictors. This step determines the accuracy of the forward model and its robustness.

First, the probability density functions of the emissivities and the geophysical parameters will be checked, to eliminate potential outliers as well as possible artefacts. Filters will be applied if necessary (related to clouds, to RFI for the emissivities).

Second, the time and space behaviors of the emissivities and geophysical parameters will be analyzed, with Hovmöller graphs for instance, for relevant transects. This will improve our understanding of the possible relationship between the emissivities and the predictors.

Third, the correlation between the emissivities and the geophysical parameters will be calculated, in terms of space and time, using correlation matrix, scatter plots, and / or correlation maps.

From these analyses, a set of predictors will be selected, driven by a solid physical understanding of the emissivity sensitivity. The snow-covered surfaces and the snow-free surfaces will be treated separately.

3.3.2. Statistical model for emissivity forward operator

This study relies on statistical models to establish links between geophysical parameters and emissivities. As highlighted in the joint analysis of emissivities and geophysical parameters, numerous geophysical parameters influence the microwave signal in a highly intricate manner, both spatially and temporally. Neural networks are particularly well-suited for this task, as they can effectively capture complex, non-linear relationships between variables. Neural networks have already been widely applied to regression problems in remote sensing and have recently demonstrated success in forward ocean emissivity modelling (Kilic et al., 2023). In this study, a compact Multi-Layer Perceptron (MLP) (Rosenblatt, 1961) is utilized, featuring only one hidden layer with a reasonable number of neurons that will depend on the predictor number. This type of neural network can be quickly trained and inferred on standard Central Processing Units (CPUs). Various configurations were tested (different number of layers and/or neurons), and the results indicate that the architecture of the MLP does not significantly alter the outcomes. The network is trained using a Bayesian regularization back-propagation algorithm, which ensures robust performance and reduces the probability of overfitting by constraining the weights of the NN (MacKay, 1992; Foresee and Hagan, 1997).

A separate neural network is trained for each frequency. To ensure a consistent relationship between the V and H polarizations, a single NN is employed to predict both simultaneously. This approach enforces coherence between the two polarizations while maintaining flexibility across different frequencies.

The data from the last ten days of each month of the initial one-year dataset of collocated geophysical predictors and satellite-derived emissivities are isolated to train the statistical model. The emissivity parameterization is then evaluated on the original data set, excluding the data used to train the NNs. Two major metrics assess the quality of the parameterization: the linear correlation coefficient R, the coefficient of determination R2 and the Root Mean Square Error (RMSE) calculated from the difference between the parameterized value and the target. Note that the systematic error (or bias) is expected to be 0 over the dataset, by construction of the NNs, and as a consequence, RMSE is very close to the Standard Deviation (StD) of the error. The probability distribution function of the parameterized and initial emissivities are also compared. Maps are shown and more detailed temporal analysis are conducted at local scale. The NN results are systematically and directly compared to the 10-day emissivity climatology. Here, we want to test the performance of the geophysically-based emissivity parameterization, as compared to a climatology derived from satellite-derived emissivity. The expectation is that a parameterization derived from geophysical variables at the time of the observations provides a better estimate than a climatology that is not linked to current surface conditions.

3.4. The snow surfaces

3.4.1. Preparation of the data specifically for the snow-covered land

A full winter season is considered, in the Northern Hemisphere (continental snow-covered extent in the Southern Hemisphere is limited). Data are collected from the beginning of October 2018 to the end of May 2019. Greenland and permanent glaciers are treated separately, as ERA5 snow information is not available in these areas. Microwave emissivities are very sensitive to the presence of open ocean, and data within 80 km of the coast are removed to avoid any contamination. A spatial and temporal interpolation is performed to collocate the geophysical parameters with the satellite-derived emissivities at swath level. Data over 10 days are aggregated onto the same Equal-Area Scalable Earth (EASE) grid 2.0 over the Northern Hemisphere at 12.5 km (Lambert’s equal-area, azimuthal) (Brodzik et al.,

2012). As already mentioned, the analysis is limited to clear-sky emissivities (with ERA5 total liquid water path < 0.05 kg m−2). Data are kept only if the Snow Depth is above 0.02 m

3.4.2. The predictor selection

Figure 1 and Figure 2 present examples of satellite-derived emissivities over snow-covered regions, along with the collocated geophysical parameters, for two contrasting periods, in the middle (1–10th January 2019) and at the end (1–10th April 2019) of the winter season. The spatial and temporal variability of the snow emissivity is observed, depending on frequency, polarization, and time of the year. As expected, the snow emissivity at a given frequency is systematically higher in the vertical polarization than in the horizontal polarization. For a given location and season, the snow emissivity tends to decrease with increasing frequency. North of Canada and Siberia, the snow emissivity significantly drops from January to April, evidencing stronger volume scattering likely due to an increase in the snow grain sizes: the higher the frequency, the larger the emissivity decrease. The decreasing of the emissivity can also be linked to a deeper snowpack leading to more volume scattering.

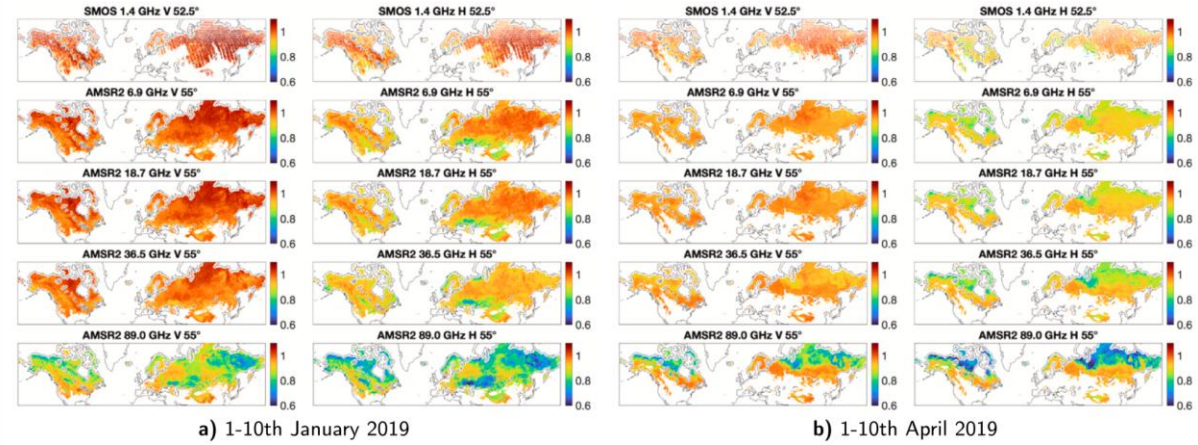

Figure 1: *Average satellite-derived emissivity over ten days for selected frequencies (at 1:30 pm for AMSR2, 6:00 am for SMOS). Only snow-covered regions are presented (Snow Depth> 0.02 m).*

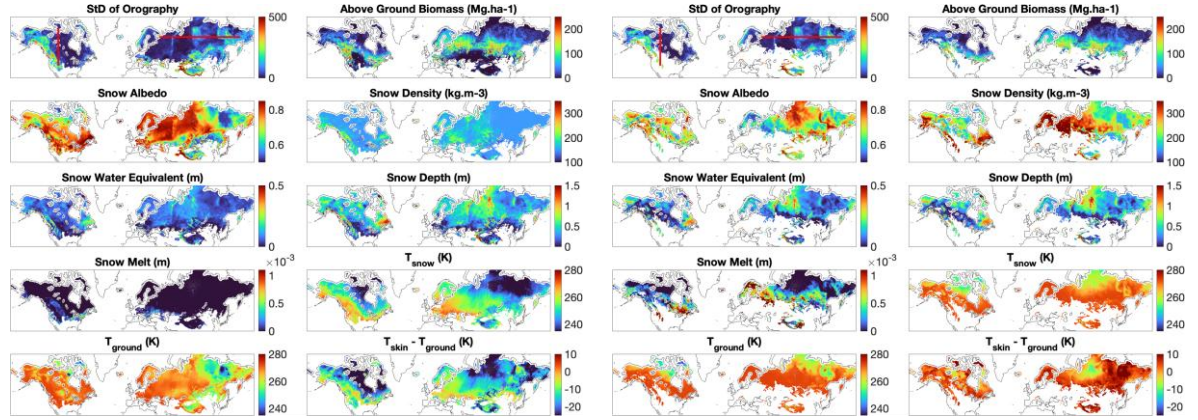

a) 1-10th January 2019 b) 1-10th April 2019

Figure 2: *Examples of average geophysical parameters over ten days at 1:30 pm. Only snow-covered regions are presented (Snow Depth> 0.02 m). The two red lines on the map of Std of Orography of the beginning of April 2019 indicate the transect studied later in the document.*

Figure 3 presents the correlation matrix between the geophysical parameters and the emissivities at different frequencies for two contrasting periods in the boreal winter (January February, and April May), over the snow-covered Northern Hemisphere (excluding Greenland, as already mentioned). During mid-winter, low-frequency emissivities exhibit strong

intercorrelation while the 36.5 and 89.0 GHz bands behave distinctly. In contrast, during the melting period, correlations among low frequencies weaken, and those among 18.7, 36.5, and 89.0 GHz strengthen. As winter progresses, snow metamorphism increases grain size (Sturm and Benson, 1997), enhancing volume scattering and lowering emissivity, even at lower frequencies later in the season. For instance, the 18.7 GHz channel transitions from low-frequency behavior in January to high-frequency characteristics by April. Correlations between snow parameters and emissivities show that Snow Depth and Snow Water Equivalent are less correlated with emissivities than Snow Density and Albedo. Linear relationships between microwave signals and Snow Depth or Snow Water Equivalent (SWE) often fail across large spatial or seasonal scales (Cordisco et al., 2006; Rosenfeld and Grody, 2000; Grippa et al., 2004). Spatio-temporal correlation coefficients indicate that Snow Depth and SWE have weak spatial correlations but may show stronger local temporal correlations with emissivities, consistent with Derksen et al. (2010), who estimated SWE from 37 GHz brightness temperature histories.

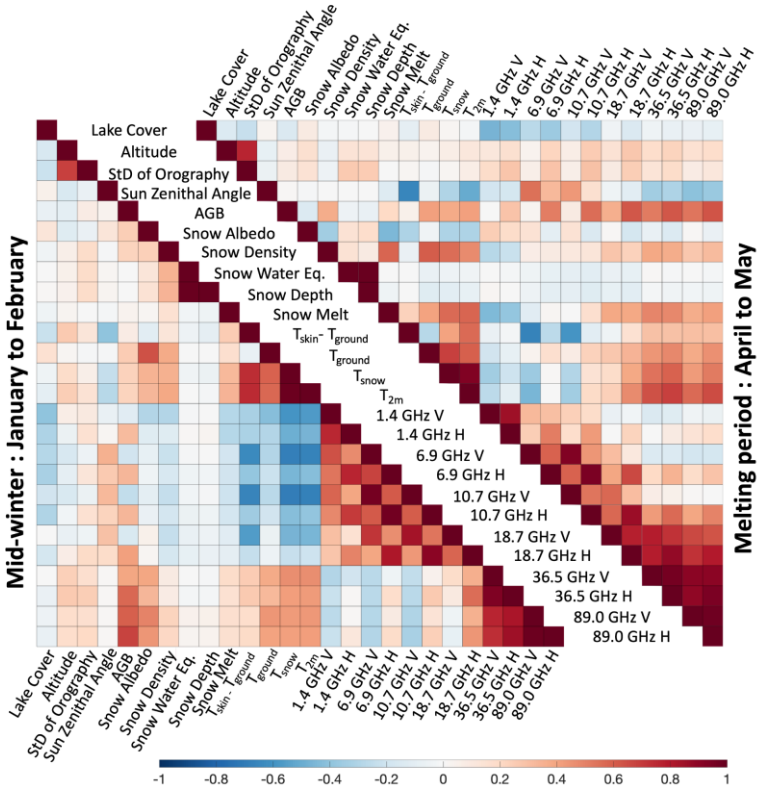

Figure 3: *Linear correlation between geophysical parameters and emissivities for both mid-winter (bottom left) and melting period (top right). AGB stands for Above Ground Biomass; Snow Water Eq. for Snow Water Equivalent*.

Hovmöller diagrams (Figure 4) along 110°W (latitude 40°-70°N) reveal a steady increase in Snow Density through winter, a key factor in snow dielectric properties (Wiesmann and Mätzler, 1999). However, correlations between Snow Density and emissivities above 36.5 GHz remain limited, while low-frequency emissivities show mid-winter anticorrelation with Snow Density. Although dry snow is generally transparent at low frequencies, Schwank et al. (2015) showed it still affects emissivity through snow-air interface effects. ERA5 provides bulk Snow Density, though actual density varies within the snowpack; new low-density layers can influence high-frequency emissivities (>100 GHz) (Sandells et al., 2024). The temperature gradient between the surface and ground (Figure 3) is anticorrelated with low-frequency emissivities but positively correlated with higher frequencies, especially in spring. This reflects both (1) the low-frequency sensitivity to ground temperature via penetration, and (2) the gradient's control on snow metamorphism, which enhances scattering and reduces high-frequency emissivity (Josberger and Mognard, 2002). Vegetation, represented by Above

Ground Biomass (AGB), shows strong, frequency-increasing correlations with emissivities during winter (Figure 3), particularly for H-polarization. Since vegetation has high emissivity and weak polarization contrast (Prigent and Jimenez, 2021), it becomes dominant where snow emissivity is low (Derksen, 2008). Figure 4 further shows that regions with AGB > 50 Mg ha^{-1} (north of 53°N) correspond to elevated emissivities at 18.7 and 36.5 GHz. Terrain relief also enhances emissivities, especially in H-polarization, and reduces polarization differences (Prigent et al., 1997; Mätzler and Standley, 2000). This is evident near 41°N and 45°N, where orographic variability is high. Finally, emissivity features linked to water bodies are prominent near 54.5°N (small lakes), 59°N (Athabasca Lake), and 68°N (the Arctic gulf). These regions exhibit low emissivities at 6.9 and 18.7 GHz (H-pol). During mid-winter, frozen or snow-covered lakes show scattering at frequencies above 18.7 GHz and high polarization differences, indicative of residual liquid water early in the season. The gulf near 68°N becomes sea ice-covered after November, producing a sharp emissivity increase. Incorporating detailed lake and water-body information is therefore essential for accurate emissivity parameterization and spatial variability representation.

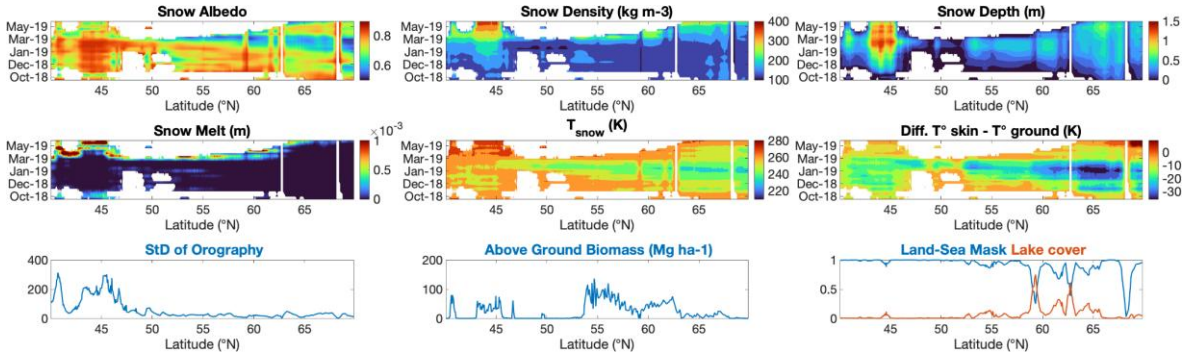

a) Geophysical parameters

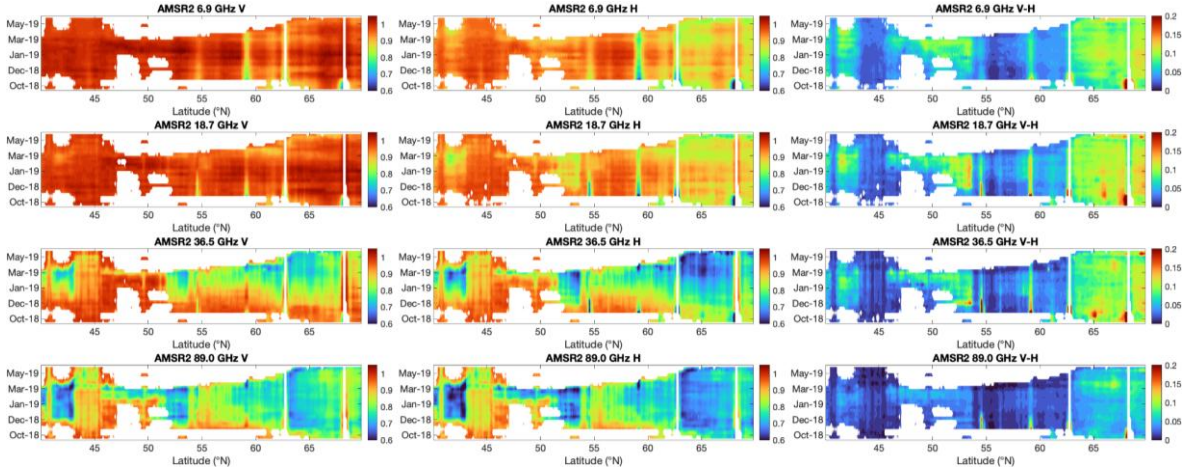

b) Microwave emissivities for the vertical and horizontal polarizations, as well as for the polarization difference (V-H).

Figure 4*: Hovmöller diagrams at 110°W, from 40°N to 70°N (red line over Canada seen in Fig 2), for both geophysical variables (a), and emissivities (b) from October 2018 to end of May 2019). Variables without seasonal variations are represented by transect. Only snow-covered areas are represented, for only some of the studied frequencies.*

3.4.3. The NN parameterization results

Following the joint analysis, a subset of geophysical variables was selected to train a neural network-based statistical model. Individual and various combinations of input parameters were

tested to determine their effectiveness, ultimately focusing on a specific configuration that balanced model simplicity with the inclusion of essential geophysical details.

Table 1 presents an overview of the 10 geophysical parameters selected for this experiment, which were chosen based on their significant relationships with passive microwave emissivities, as identified in our initial analysis.

Name	Geophysical parameters		
	Fixed	Snow	Temperature
NN 10 parameters	Lake Cover StD of Orography AGB	Albedo Density Depth Melt	Snow (T_{snow}) Ground (T_{ground}) Gradient ($T_{skin} - T_{ground}$)

Table 1: *List of geophysical parameters used as input to the emissivity parameterization over snow-covered areas.*

Climatologies of emissivities, derived from satellite time series, have been generated for each 10-day aggregation. These climatologies serve as a baseline method against which our results (i.e., the retrieved emissivities) are systematically compared. The reason for this is that we want to show that we can improve the current radiative transfer based on the use of climatological emissivities. Second, these emissivity climatologies are also considered as complementary inputs to the neural network parameterization, alongside the geophysical parameters. This is a common approach in prediction problems, where a priori knowledge of the variable to be predicted can be incorporated as a predictor to further constrain the prediction problem, if this information is available. Note that our goal is not to reproduce the climatologies, but the observed emissivities (also called target emissivities) with possible interannual variations. The climatologies act only as a first guess to guide the NN towards the correct emissivities.

Figure 5 presents the statistical results for the selected NN parameterizations, over the studied snow-covered surfaces in the Northern Hemisphere, from October 2018 to May 2019. The NN parameterization that use only geophysical parameters (yellow lines on Figure 5) achieve a correlation coefficient (R) above ~0.8 for all frequencies and polarizations, and an RMSE below ~0.03 for frequencies up to 18.7 GHz (both polarizations) and below 0.045 for higher frequencies. This represents an approximate twofold reduction in error compared to using mean emissivities for each frequency and polarization, as indicated by the ratio of 2 or more between the RMSE and the standard deviation of the initial satellite-derived emissivities (targets), shown in the top-right panel of Figure 5. The results consistently perform better for V than for H polarization, as expected from the lower emissivity variability observed at V polarization. Comparisons between the emissivity climatologies and the target emissivities (black lines in Figure 5) reveal that emissivity climatologies outperform NN parameterization using only geophysical inputs. Previous studies have demonstrated the effectiveness of emissivity climatologies in capturing the spatial and temporal variability of snow signatures at frequencies of 18.7 GHz and above (Prigent et al., 2015; Hirahara et al., 2020) on a continental scale. Incorporating emissivity climatologies as inputs to the NN parameterization (in addition to the geophysical parameters, green lines in Figure 5) improves the agreement with the target emissivities. This approach treats emissivity climatologies as a priori values for the parameterization, while the geophysical parameters add temporal variability to better represent the current environmental state for the specific winter conditions. With these additional climatological inputs, the correlation coefficients exceed 0.9 for all frequencies and polarizations, and the RMSE falls below 0.02 for frequencies up to 18.7 GHz and around 0.03 for higher frequencies. Note that R at 18.7 GHz is consistently lower than at other frequencies: this is attributed to the limited variability of emissivities at this frequency compared to higher frequencies, alongside the influence of complex scattering mechanisms.

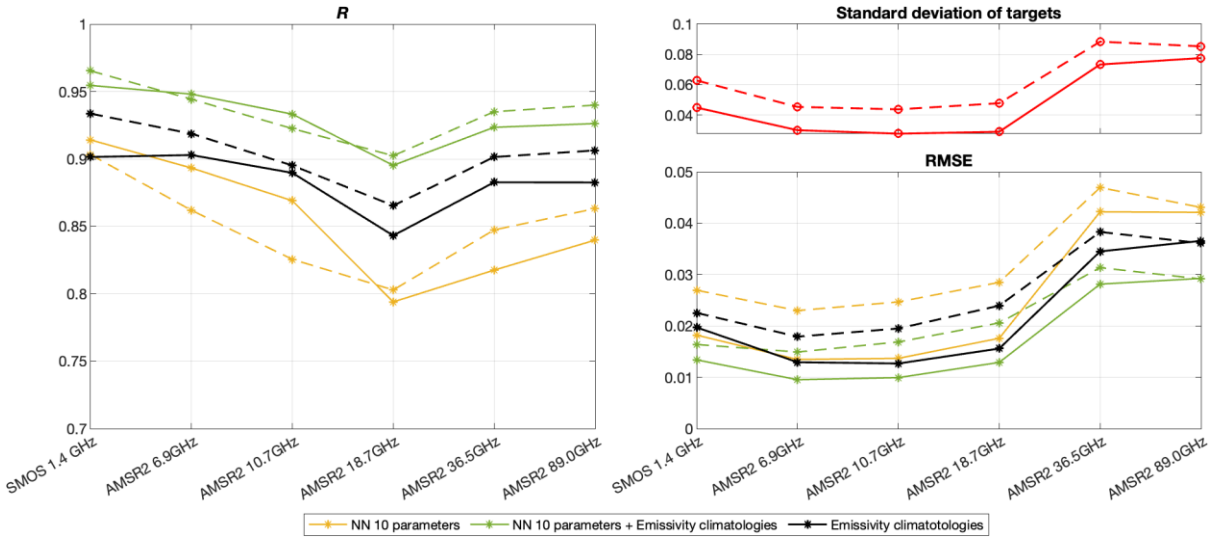

Figure 5: *Correlation R and Root Mean Square Error (RMSE) computed from the comparison of retrieved emissivities and the target values. Comparison between the emissivity climatologies and the target values is given in black. In red is given the StD of target emissivities. The solid and dashed lines correspond to V and H polarizations, respectively.*

The distributions of the retrieved emissivities (with and without climatologies) are compared to the original emissivity distributions and their climatologies in Figure 6. These comparisons reveal very similar behaviors across all frequencies and polarizations, even at high frequencies where the target emissivity variability is relatively large. The same figure also presents the distribution of emissivity errors, showing no observable biases. This represents a significant improvement over the results of radiative transfer models reported by Hirahara et al. (2020), which exhibited substantial biases, particularly at frequencies above 10 GHz.

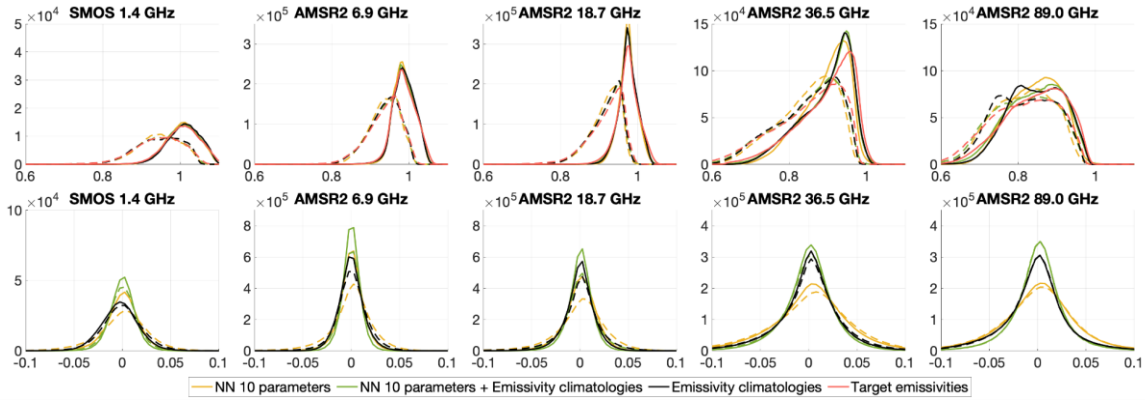

Figure 6: *Top panels: Histogram of the snow-covered surfaces emissivities from the target (red), from the climatologies (black) and from our retrievals with two configurations of inputs (10 geophysical variables only (yellow) or along with emissivity climatologies (green)). Bottom panels: Histograms of errors, i.e., targets emissivities minus the emissivity climatology in black or the retrieved emissivities in the different configuration in yellow and green. The solid lines and dashed lines represent V and H polarizations respectively.*

Finally, Figure 7 and Figure 8 present maps of the parameterized emissivities (using 10 variables with emissivity climatologies) and the differences between the target emissivities and the outputs of our method for two distinct time periods. The parameterized emissivities capture the large-scale spatial structures for both periods, even at high frequencies where pronounced latitudinal gradients are observed, influenced by complex volume scattering mechanisms. The difference maps further confirm this overall agreement, although some

regions exhibit discrepancies, particularly at higher frequencies. For more details see de Gélis et al, (2025).

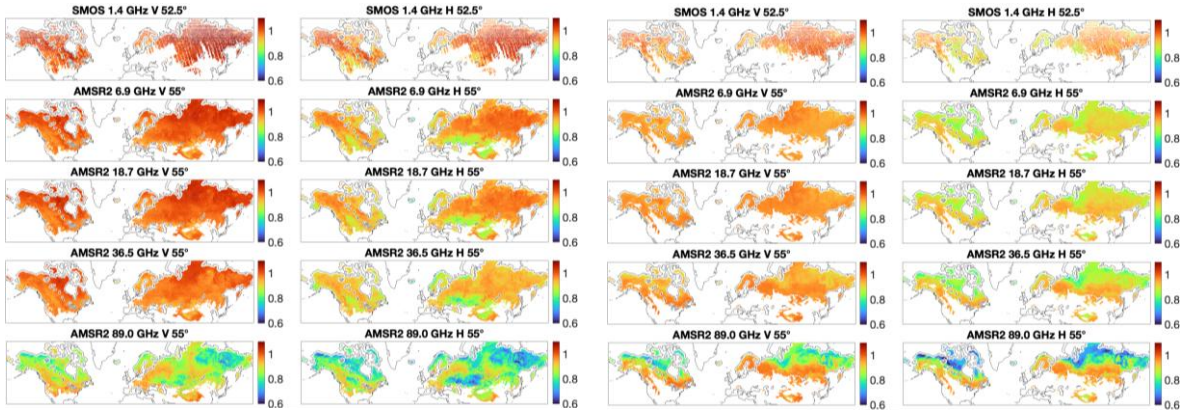

a) 1-10th January 2019 *b) 1-10th April 2019*

Figure 7: *Retrieved emissivities for ascending orbits (1.30 p.m. LST for AMSR2, 6.00 a.m. for SMOS).*

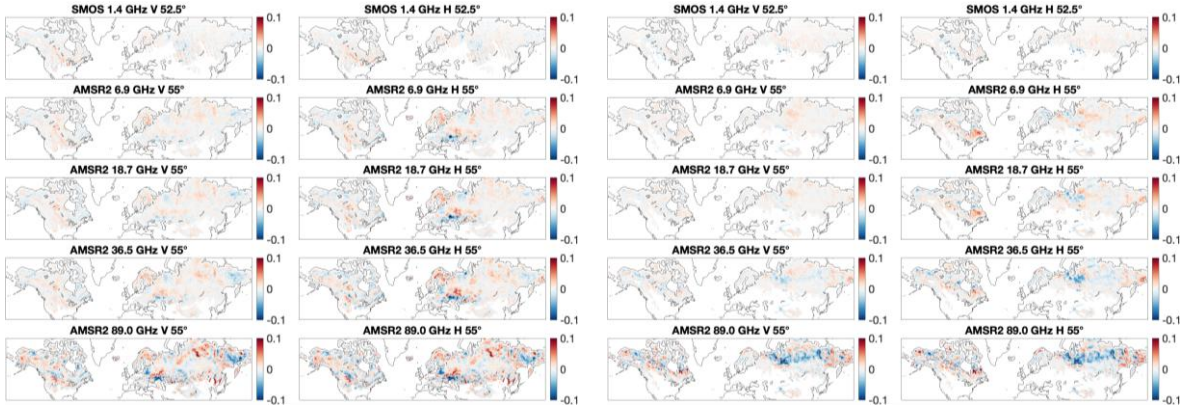

a) 1-10th January 2019 *b) 1-10th April 2019*

Figure 8*: Maps of errors, i.e., differences between target and retrieved emissivities for ascending orbits (1.30 p.m. LST for AMSR2, 6.00 a.m. for SMOS).*

A paper has been written on these results, and it has been published in Remote Sensing of Environment:

3.5. The snow-free land surfaces

3.5.1. Preparation of the data specifically for the snow-free land

Observations over snow-free land surfaces are selected for the year 2018 by retaining only those data for which the ERA5 snow depth is lower than 0.01 m. A spatial and temporal interpolation is performed to collocate the geophysical parameters with the satellite-derived emissivities at swath level. The resulting data are subsequently aggregated into 10-day averages to increase robustness and are projected onto a regular global grid at 0.125° resolution. To minimize coastal contamination, observations located within 80 km of the coastline are discarded. In addition, only clear-sky conditions are considered in order to avoid potential cloud-related biases. For each grid cell, emissivities are retained only when at least five valid observations over the 10 days are available with a total cloud liquid water path (LWP) less than 0.05 $kg \cdot m^{-2}$, based on ERA5. In cases where fewer than five observations are available, the LWP threshold is relaxed to 0.1 $kg \cdot m^{-2}$. This adaptive filtering is introduced to ensure sufficient data coverage particularly in tropical regions, where persistent cloudiness often limits the number of available clear-sky measurements. Penetrating deserts are excluded from the parameterization because the variation of emitting depth across

frequencies is not taken into account in the emissivity computation based on skin temperature. While this assumption is reasonable in most areas, it leads to large errors when not taken into account in penetrating areas such as very dry sands in deserts. Note that an emissivity parameterization for such areas is proposed in Favrichon et al. (2023). The method is based on the analysis of diurnal time series of brightness temperature and surface skin temperatures from ERA5 over the full diurnal cycle. A simplified thermal conduction model is developed to derive the sub-surface temperature profile, with the diurnal cycle of the ERA5 surface skin temperatures as a boundary condition. The emissivities and emitting depths are estimated from a minimization procedure, using radiative transfer calculations. Here, desert areas are filtered out using the aeolian aerodynamic roughness length (z0<0.15 cm) computed from ASCAT and PARASOL instruments (Prigent et al.,2012).

3.5.2. The predictor selection

For the predictor selection, our approach is to use, as much as possible, variables derived directly from the ERA5 reanalysis. However, ERA5 does not provide a parameter explicitly characterizing temporal variations in surface water extent, even though passive microwave emissivities at frequencies between 6 and 36 GHz are strongly influenced by the presence of surface water. To account for this effect, we therefore incorporate information from the Global Inundation Extent from Multiple Satellites, version 2 (GIEMS-2; Prigent et al., 2020). As GIEMS-2 is not available in near-real time, a seasonal climatology based on the period 1992–2017 was computed for use in our analysis, consistent with the constraints of NWP applications. In addition, we identified discontinuities in the land-sea mask provided within the Cerise project. To more accurately represent permanent inland water bodies, we use the Global Lakes and Wetlands Database, version 2 (GLWD-2; Lehner et al., 2025).

Figure 9 and Figure 10 illustrate examples of satellite-derived emissivities over snow-free regions and their corresponding collocated geophysical parameters for July 2018. Unlike the behavior observed over snow-covered areas at higher microwave frequencies (6–36 GHz), emissivities over snow-free land surfaces remain relatively stable, particularly in the vertical polarization. In contrast, the 1.4 GHz channel exhibits high spatial and temporal variability. For frequencies between 6 and 36 GHz, changes in horizontal-polarization emissivity are primarily driven by vegetation effects. Thereby, in this context, it is important to always analyze the emissivities by considering the difference of polarization (vertical minus horizontal emissivities), as this difference tends to approach zero in densely vegetated regions, where above ground biomass (AGB) or leaf area index (LAI) is high. At 1.4 GHz, the emissivity variability is more strongly controlled by soil moisture conditions, represented here by the Soil Water Volume (SWV). An increase in soil moisture generally reduces the emissivities.

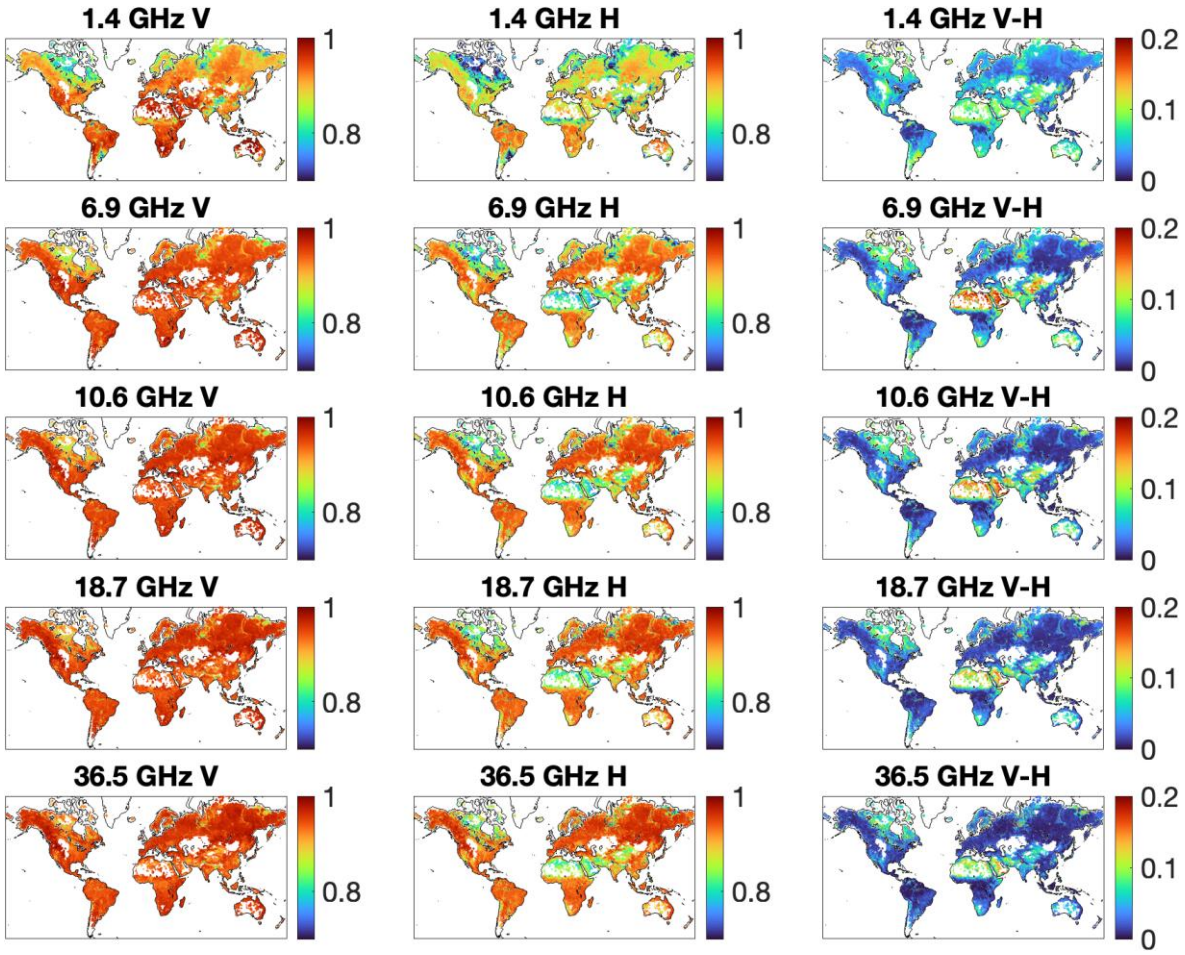

Figure 9: *Maps of emissivities at different frequencies over snow-free lands for 1-10th July 2018. The 1.4 GHz frequency corresponds to SMAP observations while higher frequencies are acquired using the AMSR2 instrument.*

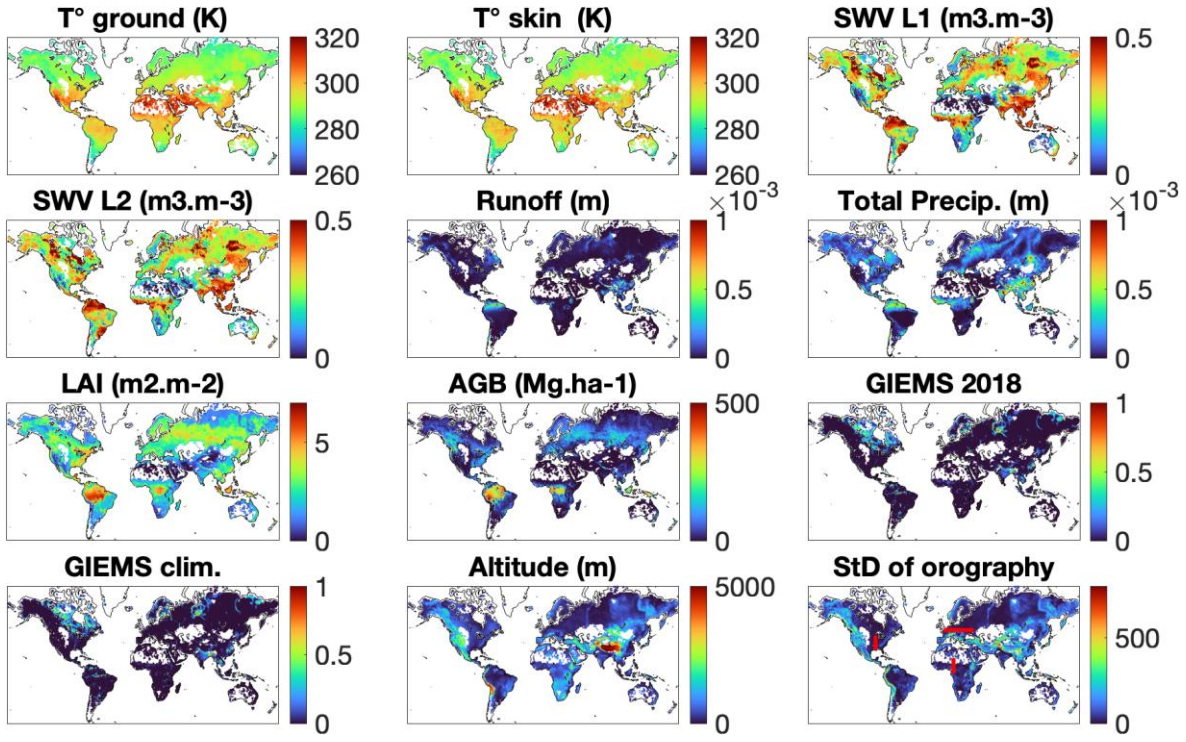

Figure 10: *Maps of geophysical parameters over snow-free lands for 1-10th July 2018. SWVL stands for Soil Water Volume Layer 1 or 2. AGB stands for Above Ground Biomass. PW is the permanent water bodies from GLWD2. Red lines on the StD of orography maps correspond to the transect studied in Figures 11, 12, 18, and 19.*

To better illustrate the spatio-temporal variability of the emissivities in relation to key geophysical variables, Figure 11 and Figure 12 present Hovmöller diagrams along two selected transects. In these figures, the GIEMS-2 inundation extent for 2018 is shown as an indicator for the presence of surface water. Figure 11 shows a transect across the Sahel region and emphasizes the strong influence of soil water volume and leaf area index on the emissivity signal. Although runoff from ECMWF could be used as a proxy for flood or drought conditions, it does not appear to correlate well with the presence of surface water during the summer period around 10°N (as indicated by the GIEMS 2018 data and the marked decrease in H-polarized emissivities). Furthermore, the comparison between the GIEMS-2 2018 values and the long-term GIEMS-2 climatology highlights that surface inundation was considerably more pronounced in 2018 than in climatological conditions. This reinforces the relevance of incorporating explicit surface water indicators into numerical weather prediction systems.

The transect shown in Figure 12, located in the southeastern United States, focuses on a region characterized by recurrent inundations of the Mississippi River. While emissivities at frequencies between 6 and 36 GHz remain relatively stable in most other regions, the presence of surface water in this area leads to a pronounced decrease in emissivity. In this case, the soil moisture indicator (Soil Water Volume) alone does not appear sufficient to capture the spatial and temporal periods during which emissivities are reduced. For instance, relatively high soil moisture values are found between 35°N and 38°N, whereas the corresponding emissivities at 1.4 GHz remain comparatively high, likely due to the influence of vegetation (as indicated by the Leaf Area Index, LAI). Once again, differences are evident between the open surface water extent provided by the GIEMS-2 climatology (GIEMS clim.) and that observed in 2018 (GIEMS 2018).

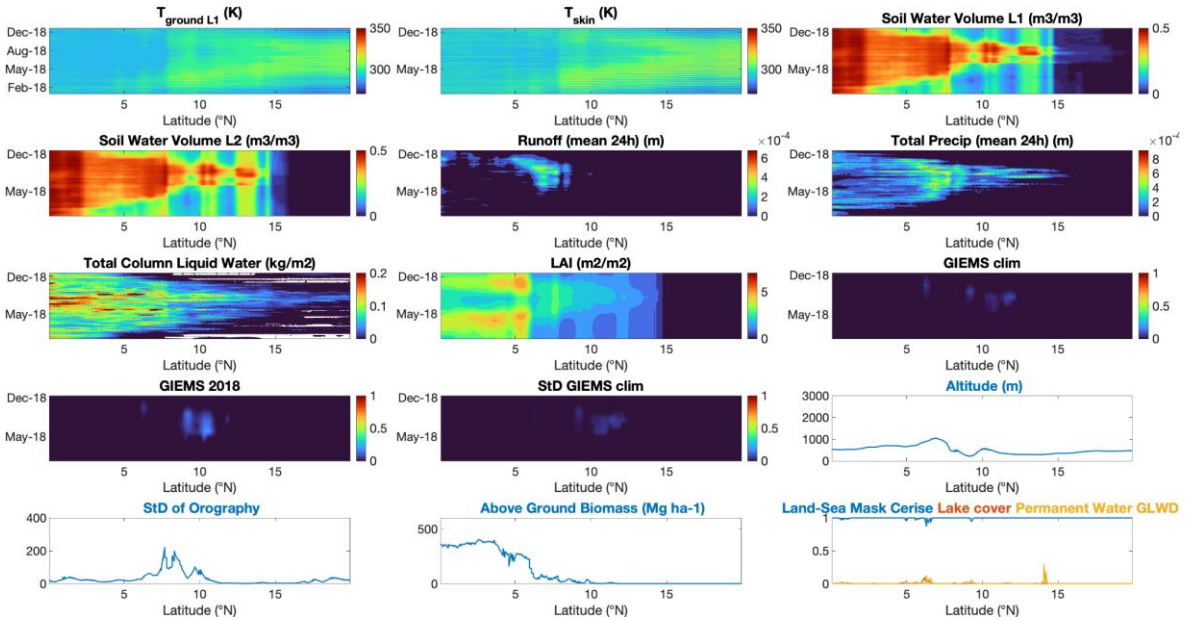

a) Geophysical parameters

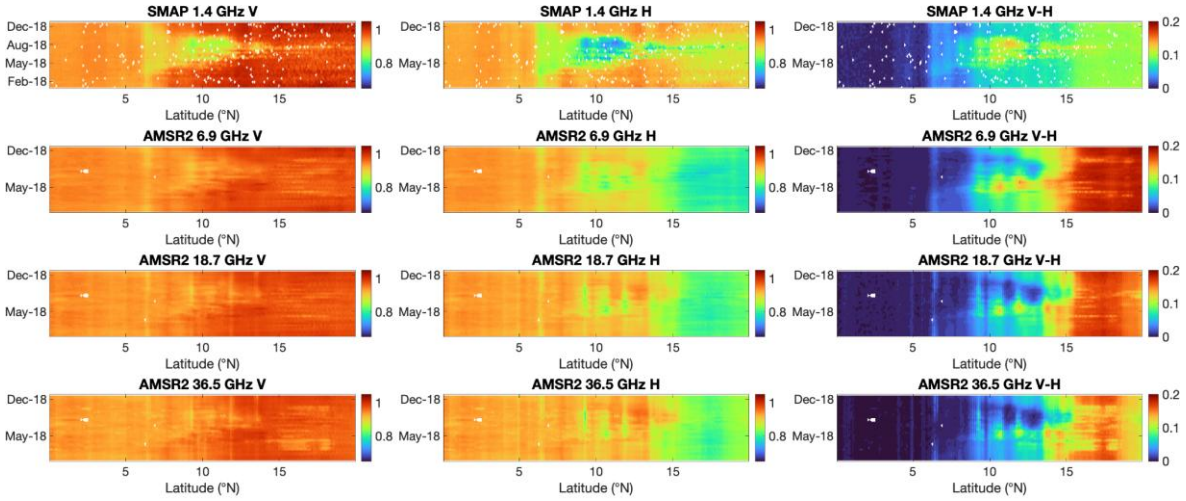

b) Microwave emissivities at different frequencies for vertical and horizontal polarizations, as well as for the difference of polarizations (V-H)

Figure 11: *Hovmöller diagrams at 13°E, from 0°N to 20°N (red line over Mid-Africa seen in Figure 10), for both geophysical variables (a), and emissivities (b) over the year 2018. Variables without seasonal variations are represented by transect. Only snow-free areas are represented, for only some of the studied frequencies*.

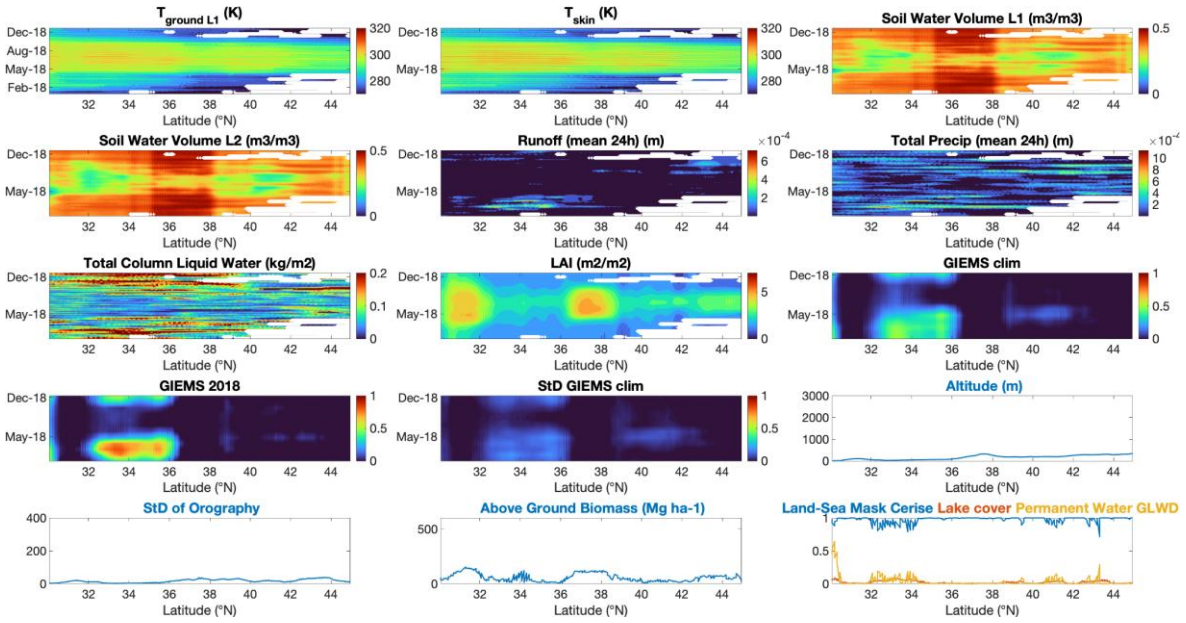

a) Geophysical parameters

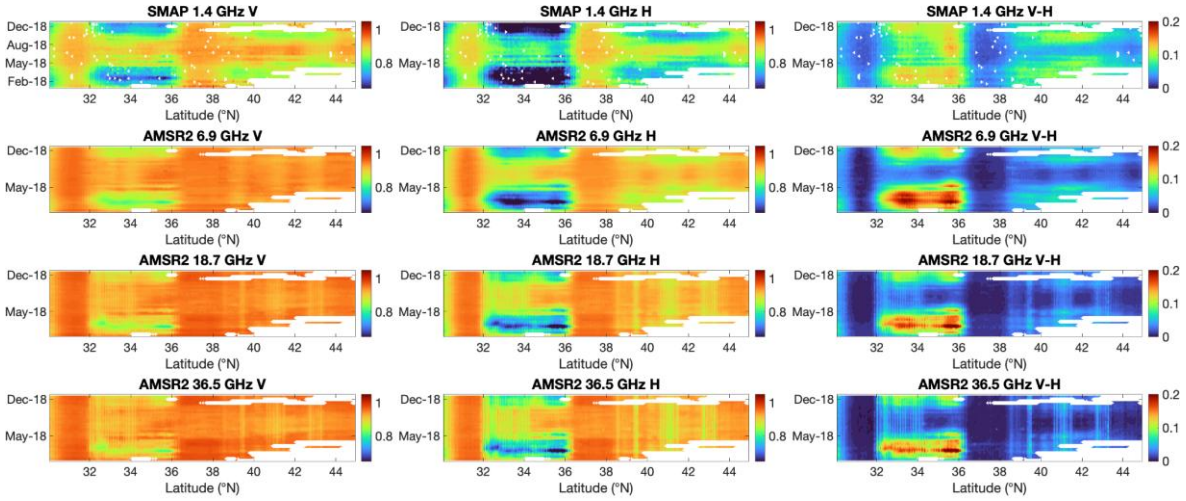

a) Microwave emissivities at different frequencies for vertical and horizontal polarizations, as well as for the difference of polarizations (V-H)

Figure 12: *Hovmöller diagrams at 91°W, from 30°N to 45°N (red line over South-East Asia seen in Figure 10), for both geophysical variables (a), and emissivities (b) over the year 2018. Variables without seasonal variations are represented by transect. Only snow-free areas are represented, for only some of the studied frequencies.*

Figure 13 shows the correlation matrix computed over the full dataset, representing the spatial and temporal correlations between emissivities at different frequencies and the various geophysical parameters. The results highlight a strong relationship between vegetation variables and horizontally polarized emissivities. Consistent with the Hovmöller diagrams, surface water extents are clearly anti-correlated with emissivities. Soil moisture also shows a pronounced negative correlation with emissivity at 1.4 GHz. At higher frequencies, however, a positive correlation is observed in horizontal polarization, likely due to the co-occurrence of high soil moisture and dense vegetation, as suggested by the strong correlation between LAI and the Soil Water Volume (Layer 1). In addition, the standard deviation of orography exhibits

a slight correlation across all frequencies. Similar to vegetation effects, surface roughness reduces the difference between vertical and horizontal emissivities.

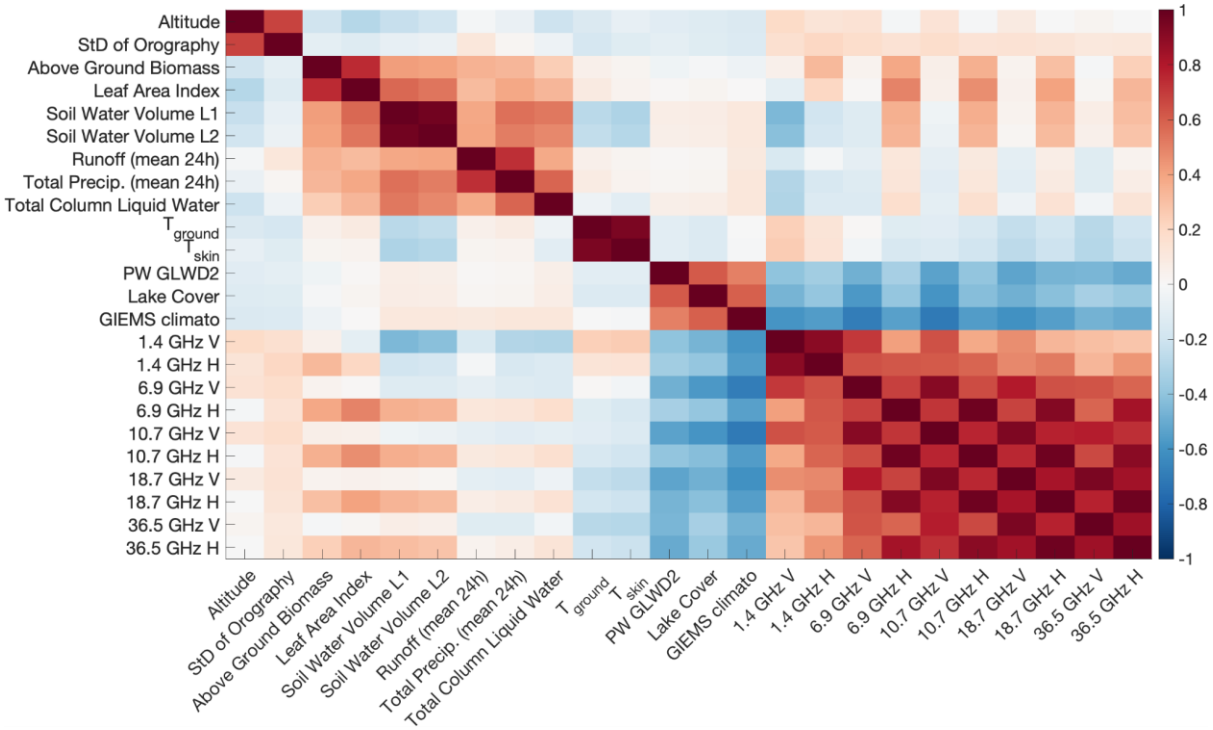

Figure 13: *Spatio-temporal correlation matrix during the full year 2018.*

To complete this analysis, Figure 14 provides density plots of LAI, soil water volume layer 1 and GIEMS climatology with emissivities. This highlights the complex relationship between emissivities and the different geophysical parameters. Even if some correlations between geophysical variables and emissivities were observed in the above analysis the link is not linear.

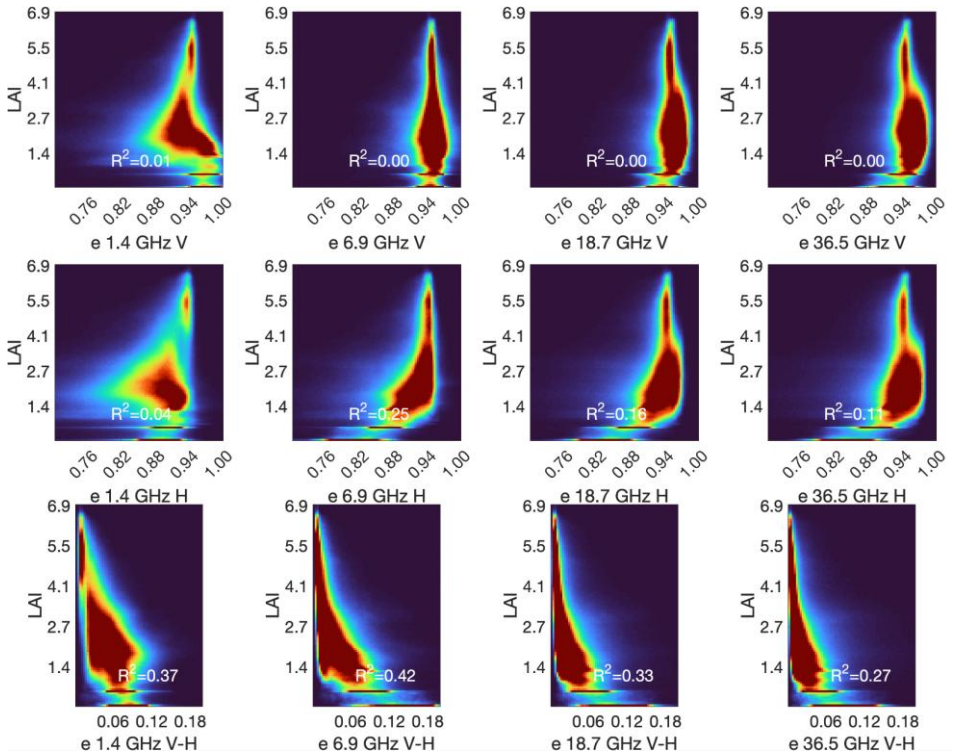

a) LAI versus emissivities. Note that horizontal lines around a LAI of 0.6 m2/m2 is presented because the distribution function of this variable is not continuous.

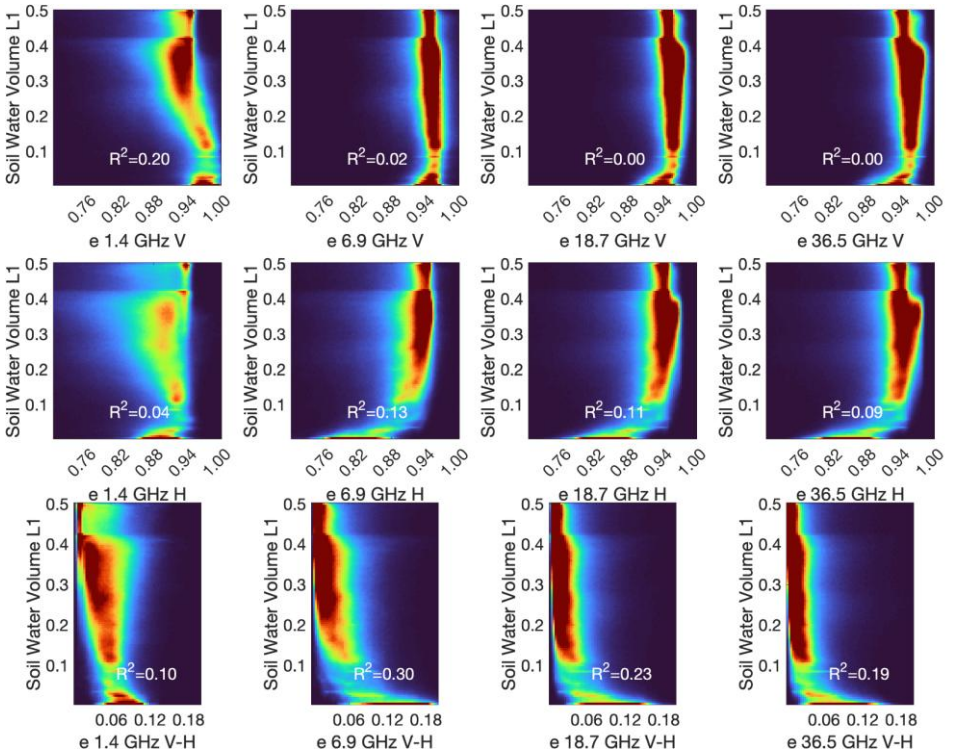

b) Soil Water Volume Layer 1 (i.e., soil moisture) versus emissivities

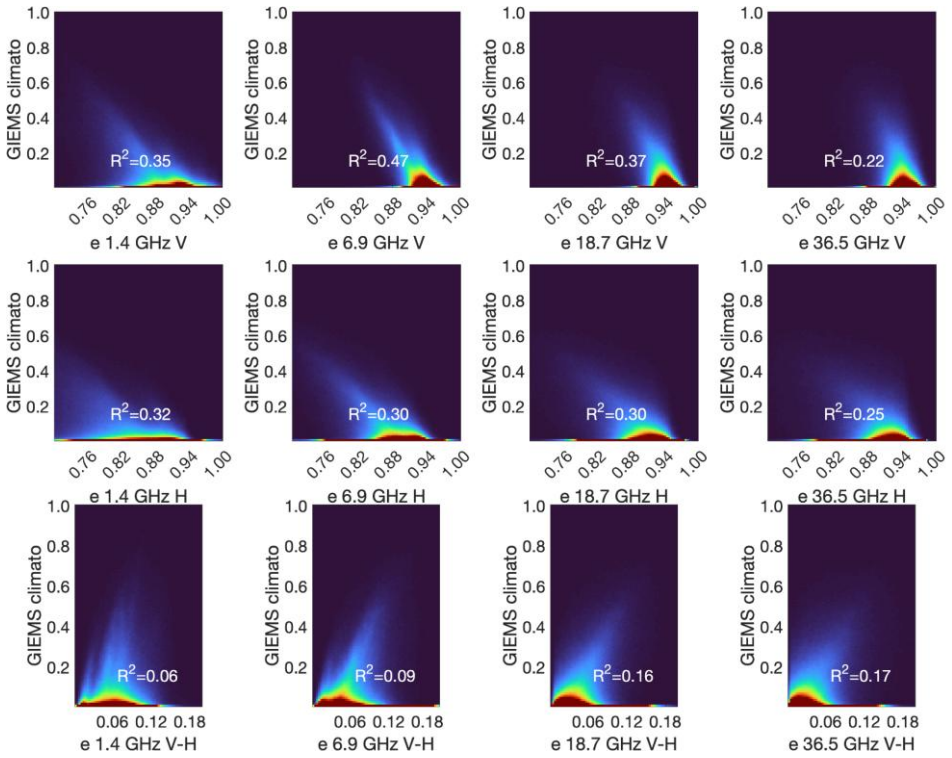

c) Climatology of flooded areas of GIEMS versus emissivities

Figure 14: *Density plots of emissivity versus some of the geophysical variables.*

3.5.3. The NN parameterization results

Following the joint analysis, a subset of geophysical variables was selected to train a neural network-based statistical model. Table 2 presents the selected geophysical parameters accounting for vegetation, surface water and soil moisture, and surface roughness. As for the snow-covered areas, different configurations were experimented and we tried to balance between model simplicity and the inclusion of essential variables. Note that AGB, permanent water (GLWD2), and StD of Orography are fixed for a given location. The LAI available in ERA5 reanalysis is an annual climatology. Thereby only the soil moisture indicator and the soil temperature are variables that are temporally dynamic. Note that the soil temperature is taken in average over the past 24 hours, and it is used as a predictor of frozen ground (not covered by snow).

Name	Geophysical parameters		
	Vegetation	Water and moisture presence	Other
NN 7 parameters	AGB LAI	**Soil Water Volume L1** GIEMS climatology Permanent Water GLWD2	StD of Orography **Soil Temperature L1**

Table 2: *Geophysical parameters selected as input to the emissivity parameterization over snow-free lands. Parameters in bold are time-varying and include interannual variability. Parameters underlined correspond to annual climatologies, meaning they exhibit intra-annual but no interannual variability. All remaining parameters are fixed.*

Similarly to the snow-covered surfaces, climatologies of emissivities derived from the satellite time series were generated for each 10-day aggregation. These climatologies are used as a reference against which the retrieved emissivities are systematically evaluated, with the objective of demonstrating potential improvements over already existing methods that rely on fixed climatological emissivities (such as TELSEM2). In addition, the climatological

emissivities are also tested as complementary predictors, functioning as a first-guess input to the neural network alongside the geophysical variables.

Quantitative results over the global testing dataset for the full year are shown in Figure 15, from 1.4 to 36 GHz. At 1.4 GHz, results are presented using SMAP observations, since the global SMOS coverage is reduced due to RFI filtering. Overall, in snow-free land conditions, the climatological emissivities provide a strong baseline, as emissivities tend to be relatively stable in time, except where surface water can occur. When the neural network is trained without emissivity climatologies as inputs, its performance does not exceed that of the climatological atlas. This is particularly evident at frequencies ≥6 GHz, where the emissivity signal is largely controlled by vegetation and surface water. However, surface water extent is not explicitly represented in ERA5, and vegetation is only available in annual climatological form. Thus, the predictors do not capture interannual variability in these key surface characteristics, limiting the potential for improving beyond climatological emissivities at these frequencies. In contrast, at 1.4 GHz the potential for improvement is larger. The emissivity at this frequency is strongly modulated by soil moisture, for which time variability is represented in the input data. As a result, the dynamic emissivity parameterization shows an added value over a purely climatological approach at L-band.

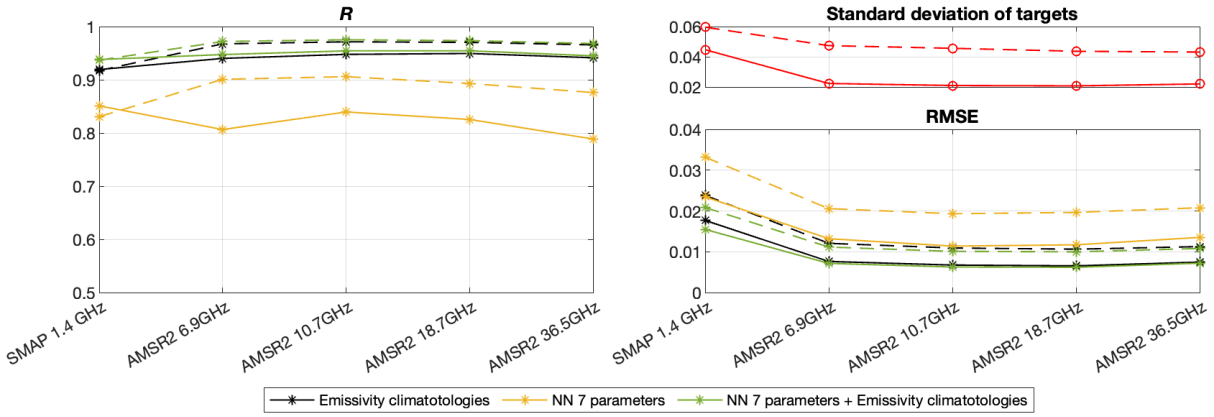

Figure 15: *Correlation R and Root Mean Square Error (RMSE) computed from the comparison of retrieved emissivities and the target values. Comparison between the emissivity climatologies and the target values is given in black. In red is given the StD of target emissivities. The solid and dashed lines correspond to V and H polarizations, respectively.*

Figures 16 and 17 present maps of differences at 1.4 GHz and 6.9 GHz between the target and the resulting brightness temperatures (BT) obtained from both neural network (NN) configurations, without and with emissivity climatologies as input, as well as those derived using climatological emissivities alone, for two distinct periods. To facilitate comparison with previous studies (e.g., de Rosnay et al., 2020), emissivities were multiplied by the skin temperature to convert them back into the brightness temperature domain. In the experiment without emissivity climatologies as NN inputs, errors generally remain within 10 K, except over northern Canada and Siberia in July, where larger discrepancies are observed.

Concerning the experiment including emissivity climatologies as inputs to the NN (Figure 16 et 17 b), together with the seven geophysical parameters, or when using the climatologies alone (Figure 16 and 17c), the differences at higher frequencies remain comparable to those at 6.9 GHz, or even smaller (typically below 3 K). At 1.4 GHz, however, localized larger errors are observed, particularly in January over the eastern United States near the snow boundary. In this region, the parameterized BTs clearly outperform the climatological estimates, as the inclusion of soil moisture provides valuable information in areas with strong interannual variability. Some residual errors are also found along the Mississippi River, even at 6.9 GHz, although the parameterized BTs still show slightly improved performance. As shown in Figure 12, comparison with the GIEMS surface water data in early January indicates that surface water extent in 2018 was lower than in the corresponding GIEMS climatology. The absence

of near-real-time surface water information likely limits the model's ability to reproduce the observed BT and emissivity signatures associated with flooding events. In such areas, only soil moisture is available as a time varying input variable; however, as illustrated in Figure 12, soil moisture and open surface water are not redundant and each provides distinct information necessary for accurately predicting BTs. Similar discrepancies observed over the Paraná Basin in South America and across parts of India in July can be explained by the same limitations.

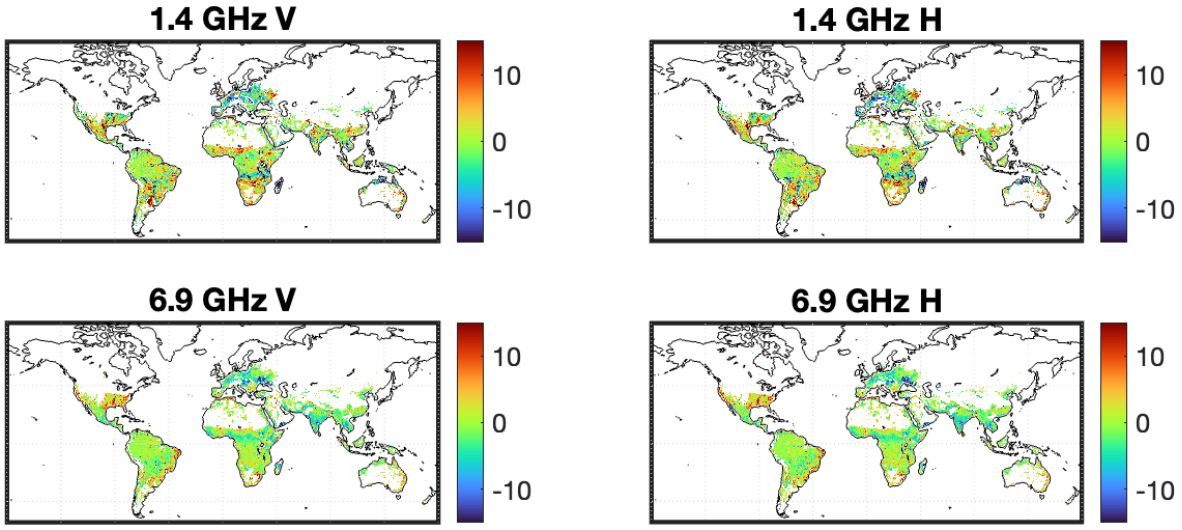

a) Difference between target and retrieved BT (NN 7 parameters)

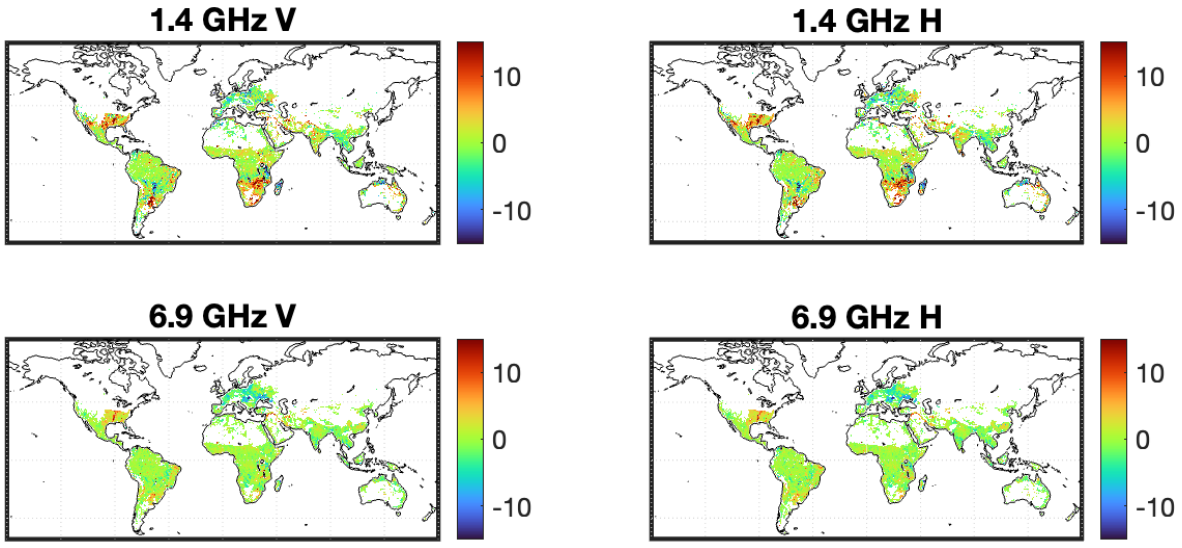

b) Difference between target and retrieved BT (NN 7 parameters + emissivity climatologies as input)

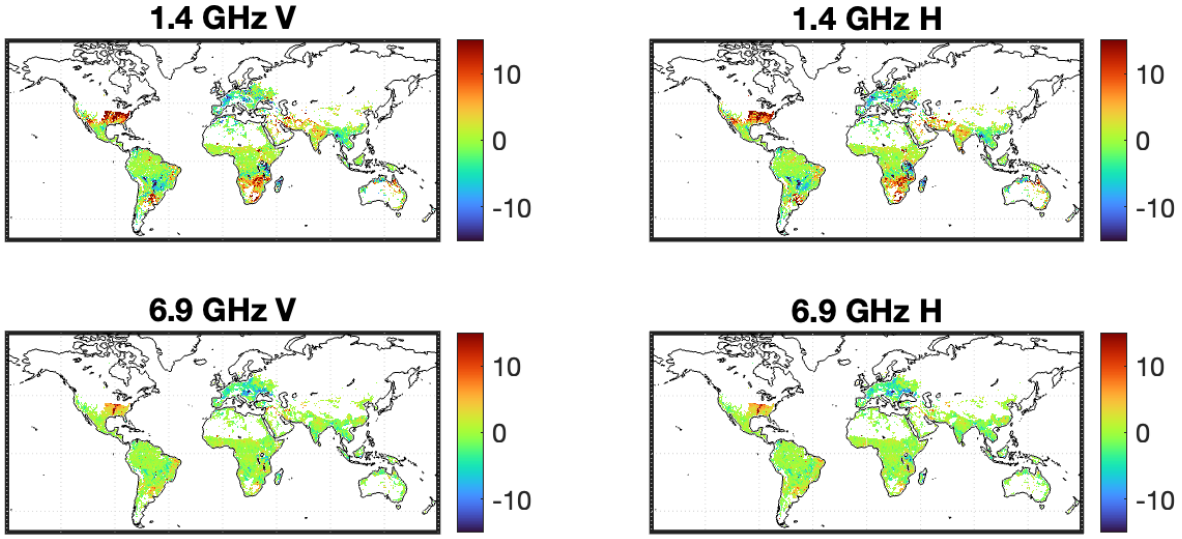

c) Difference between target and climatologies

Figure 16: *Maps of errors for the 1-10th of January 2018, i.e., differences between target and retrieved brightness temperatures with the NN based on 7 geophysical parameters as input (a), or retrieved brightness temperatures with the NN based on 7 geophysical parameters and emissivity climatologies as input (b) or climatologies directly (c).*

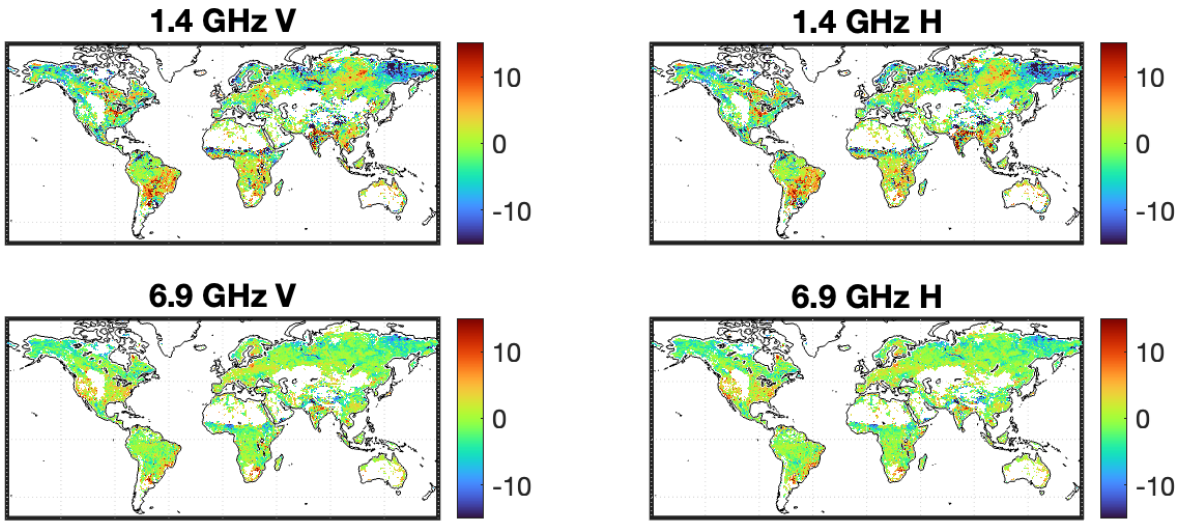

a) Difference between target and retrieved BT (NN 7 parameters)

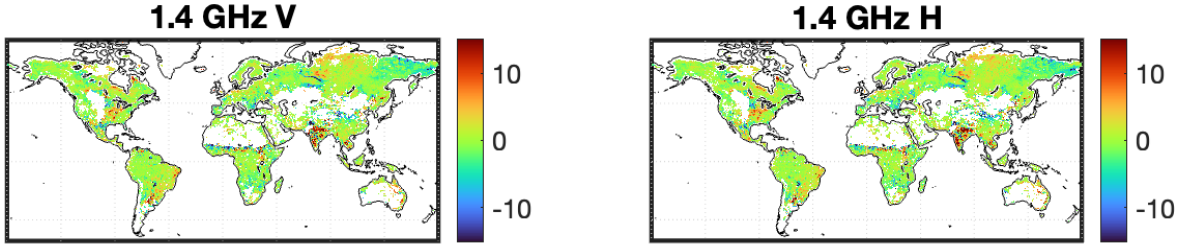

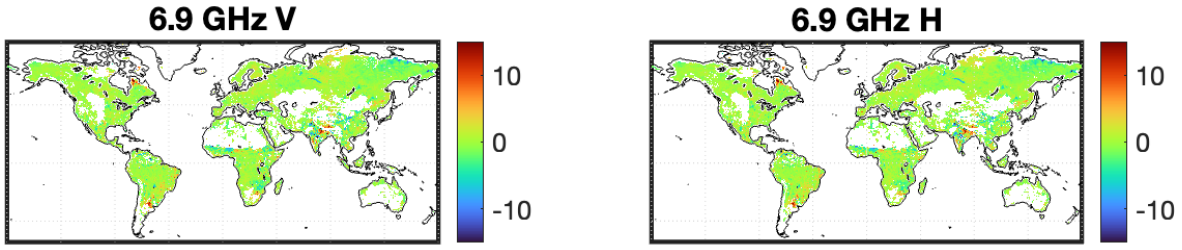

b) Difference between target and retrieved BT (NN 7 parameters + emissivity climatologies as input)

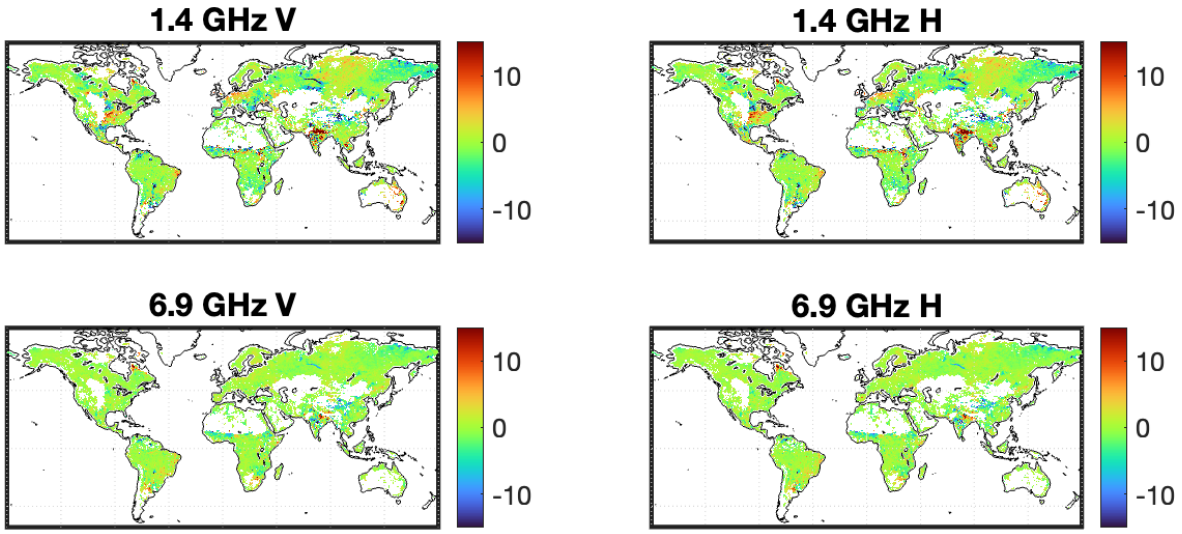

c) Difference between target and climatologies

Figure 17: *Maps of errors for the 1-10th of July 2018, i.e., differences between target and retrieved brightness temperatures with the NN based on 7 geophysical parameters as input (a), or retrieved brigthness temperatures with the NN based on 7 geophysical parameters and emissivity climatologies as input (b) or climatologies directly (c).*

To complement this analysis, a more localized comparison is provided through the Hovmöller diagrams shown in Figures 18 and 19. In Figure 18 (at 1.4 GHz), the improvement of the parameterized emissivities (Fig. 18b) over the climatological values (Fig. 18c) is clearly visible. At higher frequencies, the climatological emissivities already provide very accurate results, and the advantage of the dynamic emissivity parameterization becomes less apparent. Figure 19 highlights that the largest errors occur in regions subject to potential flooding, for example along the Mississippi River between 32°N and 36°N, and in May between 39°N and 42°N. In other parts of the Hovmöller diagrams, the results appear consistent and accurate, confirming the robustness of the parameterized approach under stable surface conditions.

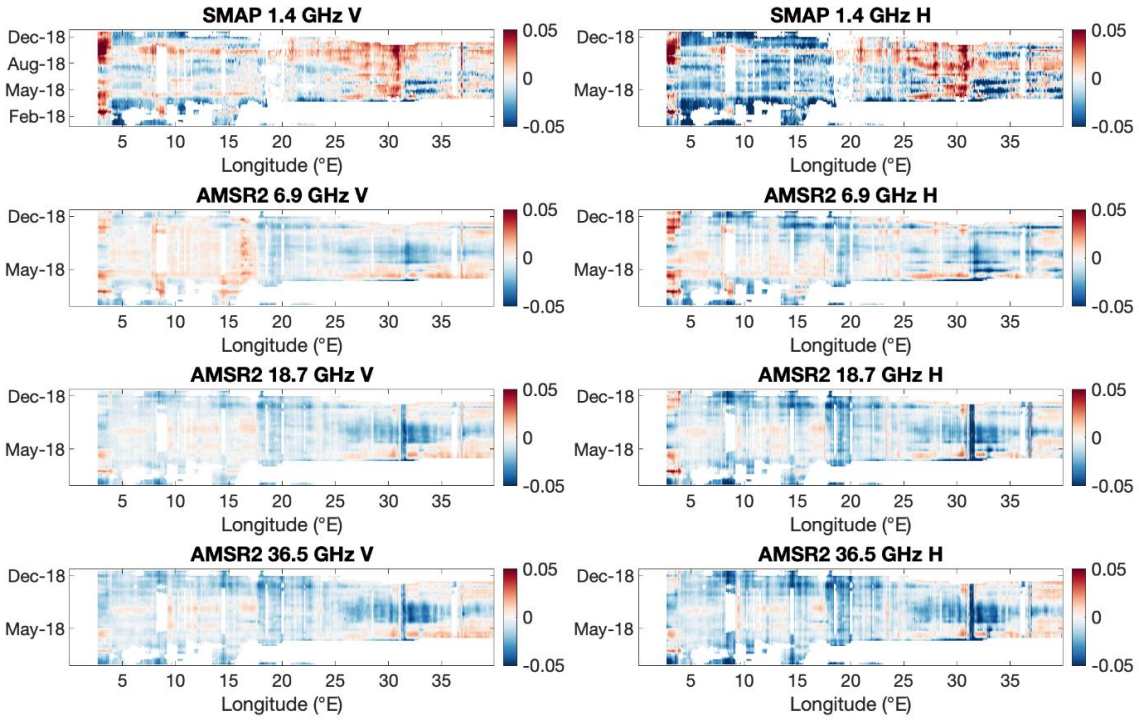

a) Difference between target and retrieved emissivities (NN 7 params.)

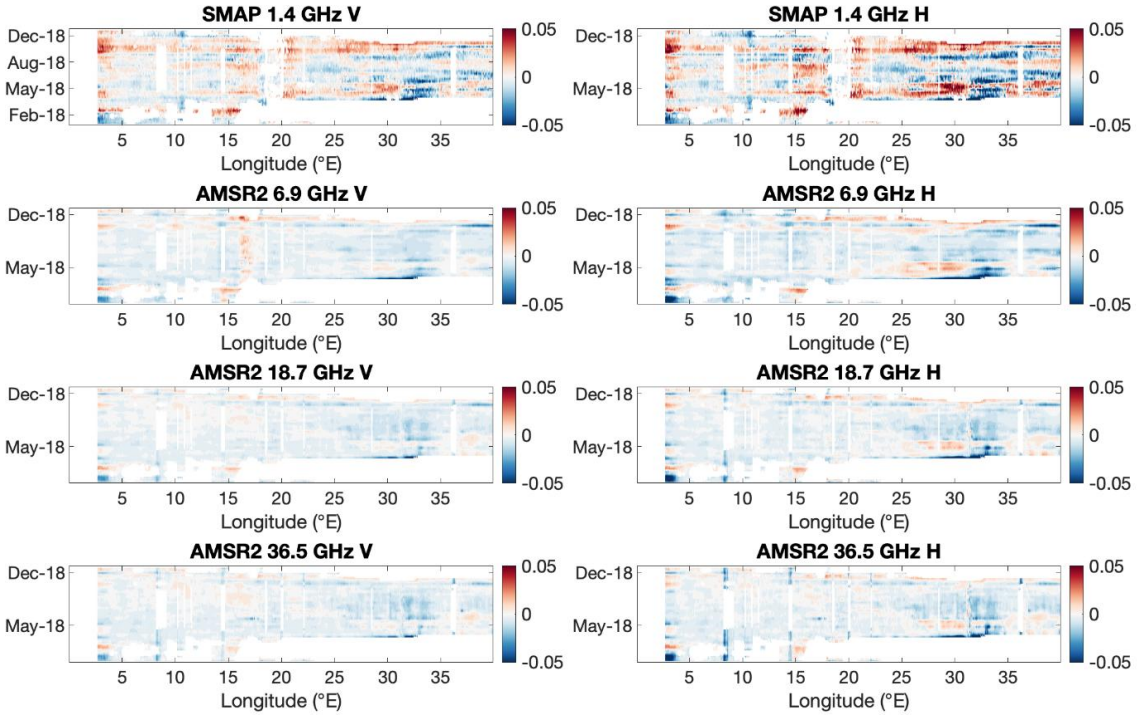

b) Difference between target and retrieved emissivities (NN 7 params. + climato.)

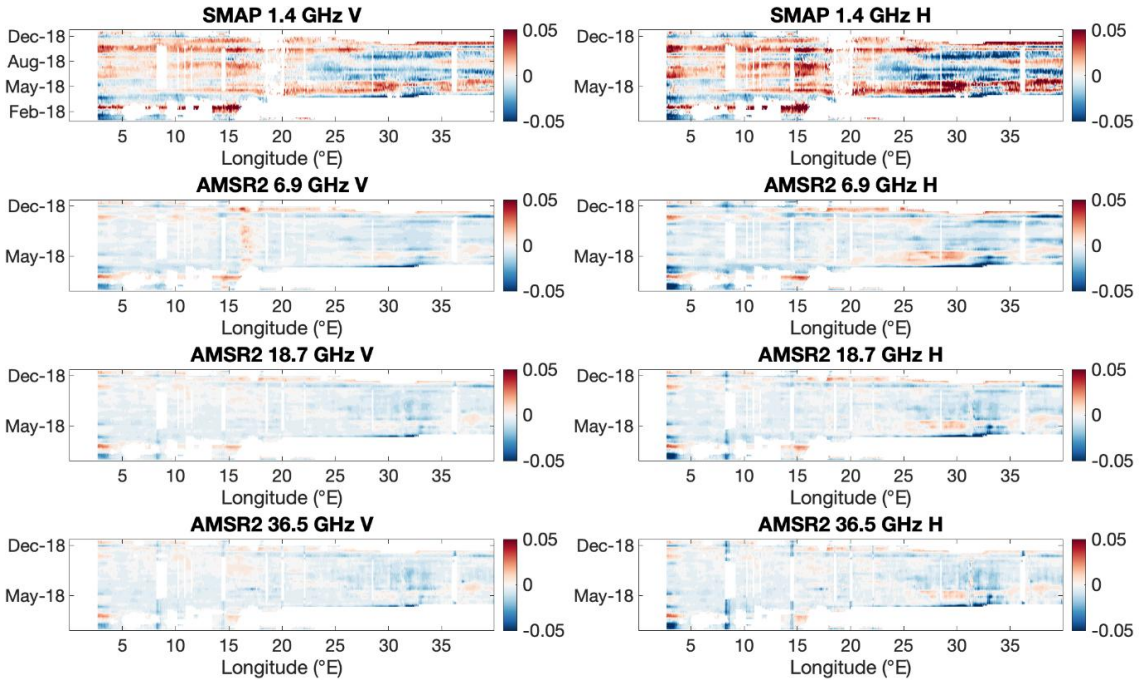

c) Difference between target and emissivity climatologies

Figure 18: *Hovmöller diagrams at 25°N, from 0°E to 40°E (red line over Europe seen in Figure 10), for both differences between target and retrieved emissivities (a and b), or emissivity climatologies (c) over the year 2018.*

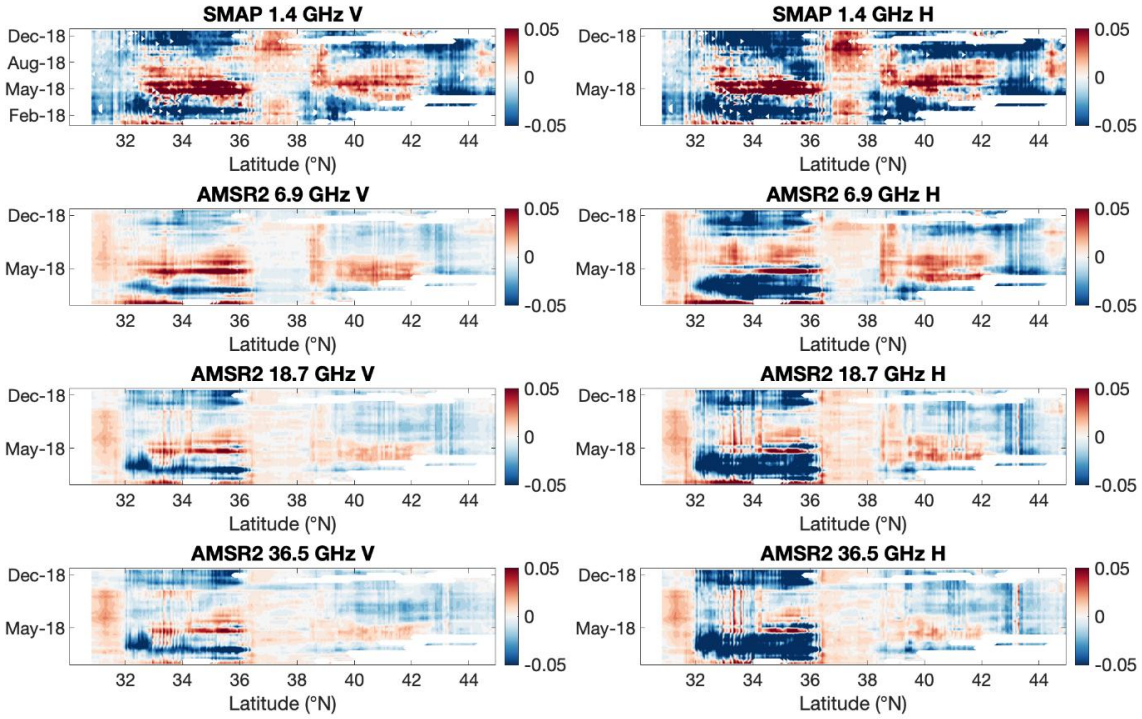

a) Difference between target and retrieved emissivities (NN 7 params.)

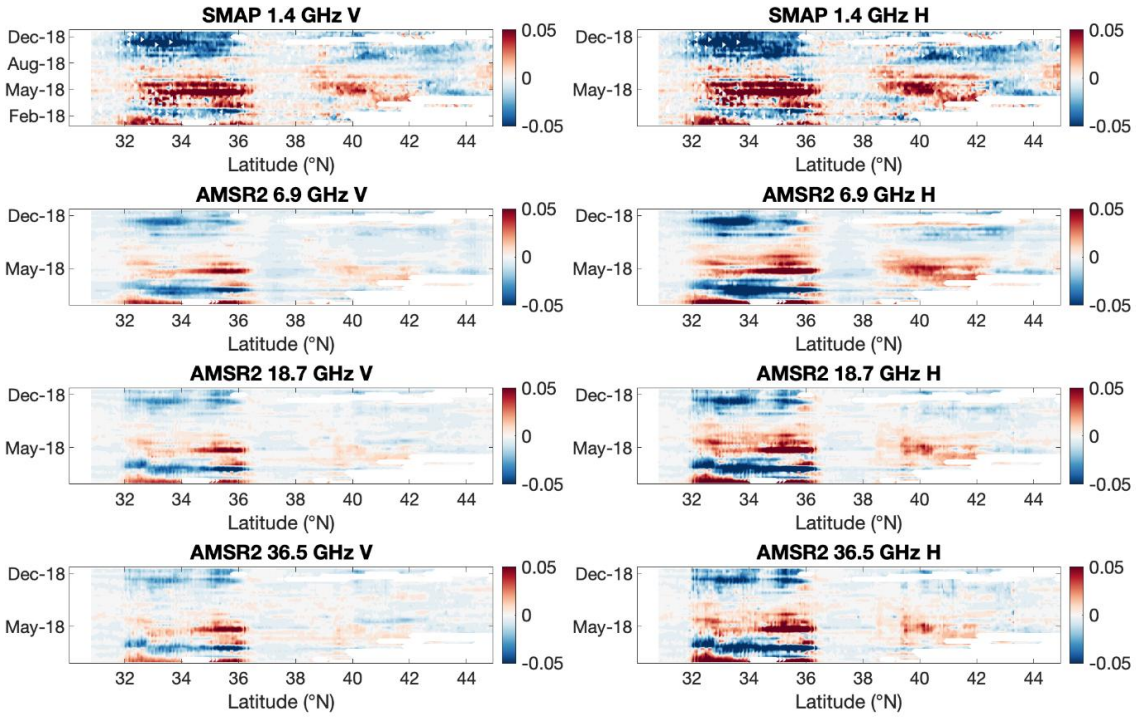

b) Difference between target and retrieved emissivities (NN 7 params. + climato.)

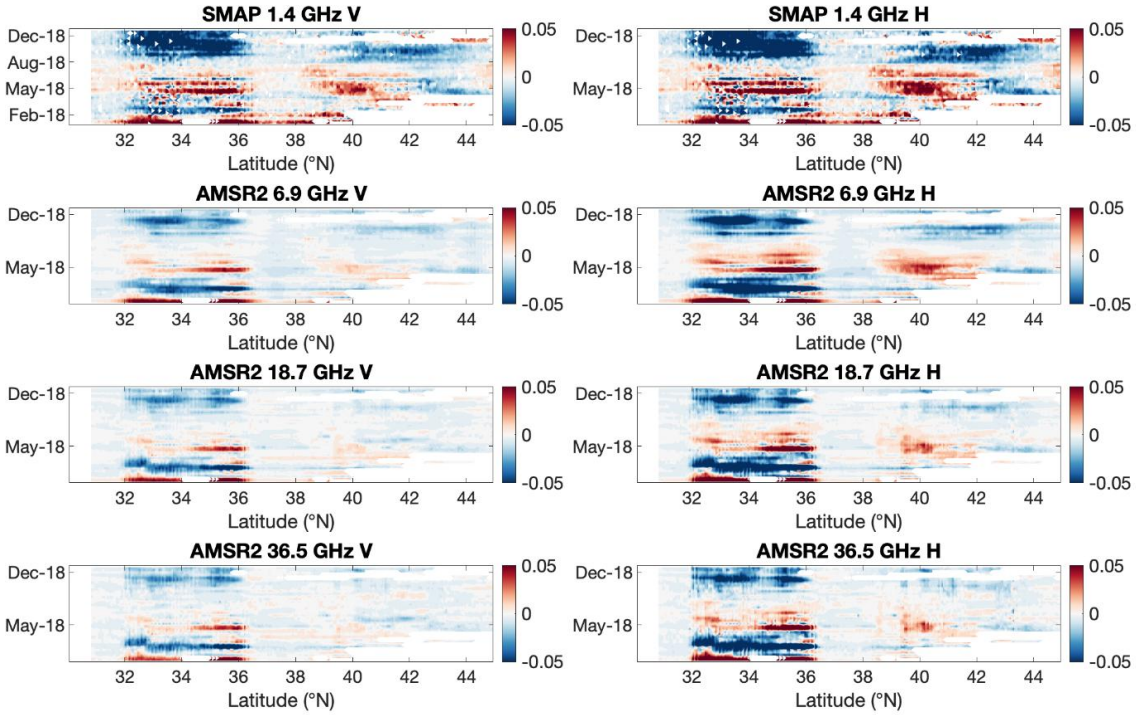

c) Difference between target and emissivity climatologies

Figure 19: *Hovmöller diagrams at 91°W, from 30°N to 45°N (red line over South-East US seen in Figure 10), for both differences between target and retrieved emissivities (a and b), or climatologies (c) over the year 2018. Corresponding geophysical variables and target emissivities are provided in Figure 12.*

3.6. Conclusion

Satellite-derived microwave emissivities were computed from AMSR2, SMAP, and SMOS observations over several years by removing atmospheric contributions and surface temperature effects using geophysical fields from the ERA5 reanalysis. The relationships between these satellite-derived emissivities and the relevant environmental parameters were then analyzed in order to identify the most informative predictors for the emissivity parameterization. Based on this analysis, a large training database of coincident emissivities and geophysical parameters was assembled to develop a neural-network (NN) emissivity parameterization capable of providing robust emissivity estimates at continental scale. Existing physical models are generally unsuitable for this purpose, as they rely on detailed ground or snow properties that can only be obtained through in situ measurements. While emissivity climatologies offer reliable baseline estimates, they do not capture the actual instantaneous state of the surface. The proposed approach therefore links globally available geophysical properties with robust satellite-derived emissivities through neural networks.

In both the snow-covered and snow-free contexts, the results show that including emissivity climatologies as inputs, in addition to the geophysical parameters, helps guide the network toward more accurate emissivity estimates. Over snow-covered surfaces, most of the global geophysical variables available are only weakly related to snow emissivity and carry substantial uncertainties, which explains the need to provide emissivity climatologies as part of the input. In this configuration, the correlation coefficient R exceeds 0.9 for all studied frequencies and both polarizations, with RMSE values below 0.02 for frequencies up to 18.7 GHz and around 0.03 for 36.5 and 89.0 GHz, and no significant bias.

Over snow-free land surfaces, the NN results obtained without emissivity climatologies as input are already very accurate from 6.9 GHz upward, with RMSE values below 0.02 in horizontal polarization and around 0.012 in vertical polarization. Including emissivity climatologies further improves the performance: global metrics show RMSE values below 0.01 for both polarizations at all frequencies between 6.9 GHz and 36.5 GHz. It is important to note that climatologies alone, i.e., without any dynamic emissivity parameterization, already provide highly accurate estimates. Although small local improvements can be observed when using the dynamic parameterization, no major enhancement is expected for two main reasons. First, because of the inherently low temporal variability of emissivities at these frequencies, climatological values are already very reliable. Second, the geophysical inputs that drive emissivity variability at such frequencies (notably open surface water and vegetation structure) are not represented in ERA5 in a form suitable for capturing day-to-day changes. Open surface water is absent, and vegetation information (via LAI) is provided only as an annual climatology. As a consequence, the NN does not have access to the near-real-time surface descriptors needed to imprint meaningful sub-seasonal variability onto the emissivity estimates, limiting the potential improvement over climatological atlases.

At 1.4 GHz, emissivity variability over snow-free areas is larger. At this frequency, the RMSE of the experiment without any contribution from the emissivity climatology is around 0.032 and 0.022 for horizontal and vertical polarizations, respectively. When emissivity climatologies are included as inputs, the RMSE decreases to below 0.02 for both polarizations. Here, the benefit of the dynamic emissivity parameterization over the climatology alone is more substantial because the key geophysical driver of emissivity at 1.4 GHz, soil moisture, exhibits real temporal variability in ERA5, enabling the NN to capture day-to-day changes in surface conditions.

The codes developed for the emissivity parameterization are available, and constitute the foundation for the two forthcoming fast surface emissivity models (SURFEM) dedicated to land and snow surfaces, which will complement the existing SURFEM-Ocean model (Kilic et al., 2023). The description of the codes is given in Annex I (Section 6).

Note that a similar methodology has been developed to parameterize the sea ice emissivity. However, as ERA5 or the IFS has very limited information on the sea ice (only its fractional

coverage at that point), outputs from the sea ice model neXtSIM have been adopted as predictors for the model of Kilic et al (2025).

4. ML-based observation operator for use in a regional coupled assimilation system

4.1 Background

Passive microwave observations contain a wealth of information of the land surface, e.g. soil temperature and moisture content. This information could be explored in land surface modelling to correct for model deficiencies, like missing precipitation. To explore these observations in land surface data assimilation we would need a mapping from the land surface state to the satellite observations. This is done with forward models or observation operators. Physical forward models could be limited by parameterizations and errors in auxiliary data. In the microwave range of the electromagnetic spectrum surface sensitive channels have large footprints e.g. 40 km around L-band (1.4GHz). Limited area models (LAMs) and regional reanalysis are operating at a resolution of 2.5 km or even finer. To address this representativity problem we suggest training a graph neural network that takes into account the sub-footprint heterogeneity of the land surface model.

In this report we present the developments done for the regional machine learning observation operator, the text is based on a manuscript in preparation for publication by Blyverket et. al 2025.

4.2 Data and methods

4.2.1 Land surface model and forcing data

The SURFEX land surface modelling framework (Masson et al., 2013), is used to create the features in the training database. The land surface model is set up with two patches, representing low and high vegetation, respectively. For the soil we use the ISBA model (Noilhan and Mahfouf, 1996). More specific for the soil we use ISBA-DF scheme (Decharme et al.,2011), which models 1D water diffusion in the soil column and Fourier's law for heat transport. The soil is discretized into 14 layers with the same layering as in Albergel et al. (2017). For the high vegetation patch we use the explicit canopy option (MEB) (Boone et al., 2017; Napoly et al., 2017).
For the snow we use the ISBA explicit snow scheme (ISBA-ES) which is a multi-layer snow scheme (here 12 layers) (Decharme et al., 2016). It solves for 5 prognostic state variables; snow water equivalent, snow heat content, density, age and albedo.
To drive the land surface model we use forcing from i) the MET Nordic analysis, available on thredds (https://thredds.met.no/thredds/catalog.html) and the CARRA (Schyberg H. et al., 2021) regional reanalysis. The CARRA data are fetched from MARS and converted to forcing files that can be utilized by SURFEX through the pysurfex framework. We use 2m temperature and humidity, 10m wind-speed, wind direction, incoming longwave radiation, and diffuse and direct incoming shortwave radiation. The ISBA model is run in an open-loop mode, which means that no data assimilation is applied. The forcing is bilinearly interpolated to the SURFEX grid and the model interpolates the hourly forcing values to the 10 minute timestep.

4.2.2 Satellite observations

In our analysis we use observations from the AMSR2 sensor. This instrument sits onboard the GCOM-W1 Japan Aerospace Exploration Agency (JAXA) satellite. It measures passive microwaves in vertical and horizontal polarization at the following frequencies: 6.925, 7.3, 10.65, 18.7, 23.8, 36.5 and 89.0 GHz. The satellite swath width is 1450 km with an incidence angle of 55°. It follows a polar orbit with overpasses at 1:30 am and 1:30 pm local time. In our

study we focus on frequencies that are sensitive to land surface variables, especially soil temperature and water content, and the snow state. We therefore use 10.65, 18.7 and the 36.5 GHz channel. We use level 1 data from JAXA, it contains swath data with locations and spatial resolution ranging from ~7 to ~40 km depending on frequency, see Table 3 for details. We will refer to the different channels as 10GHz, 18GHz and 36GHz from now.

Table 3: *AMSR2 frequencies in this study and their characteristics. Grid points within a node are related to the machine learning observation operator and will be explained later.*

Frequency	**10.7 GHz**	**18.7 GHz**	**36.5 GHz**
Footprint (km)	42 x 24	22 x 14	12 x 7
Grid points within a node	80	25	4

4.2.3 Sensitivity analysis

We want to build a forward model that could be applied for data assimilation for both snow covered and snow free surfaces. To explore which variables are related to the AMSR2 observations for the different seasons we perform a sensitivity analysis. Here we look into how the ISBA land surface variables (LSVs) correlate with the AMSR2 observations. We split the analysis into a winter case December, January and February (DJF), which is the snow accumulation season and a snow melt season in March, April and May (MAM), where the snow is melting and contains liquid water. Finally, we consider a summer period June, July and August (JJA), where we expect that the AMSR2 observations are sensitive to surface soil moisture and temperature. We compute spatio-temporally aggregated correlation values between the ISBA LSVs and AMSR2 observations at different frequencies. We also compute temporal correlations in observation space, where we have gridded the LSVs within an AMSR2 footprint and report the correlations on a map.

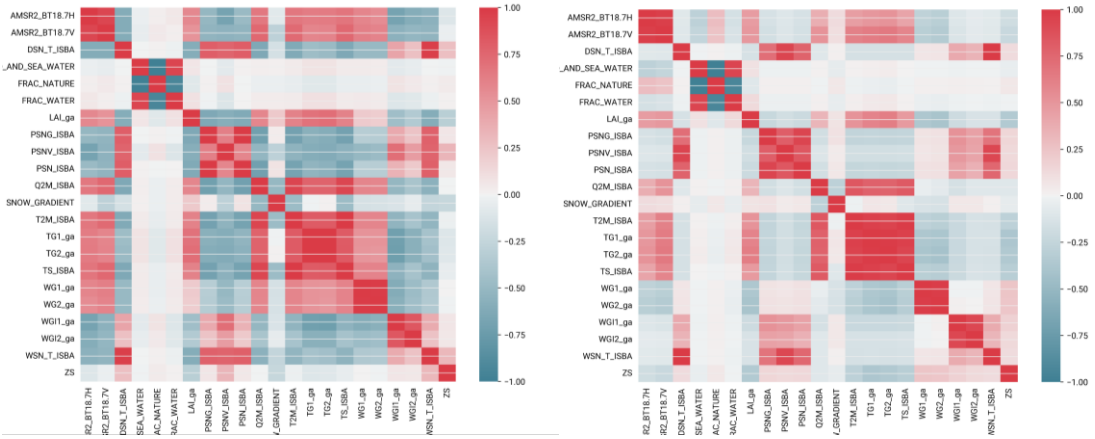

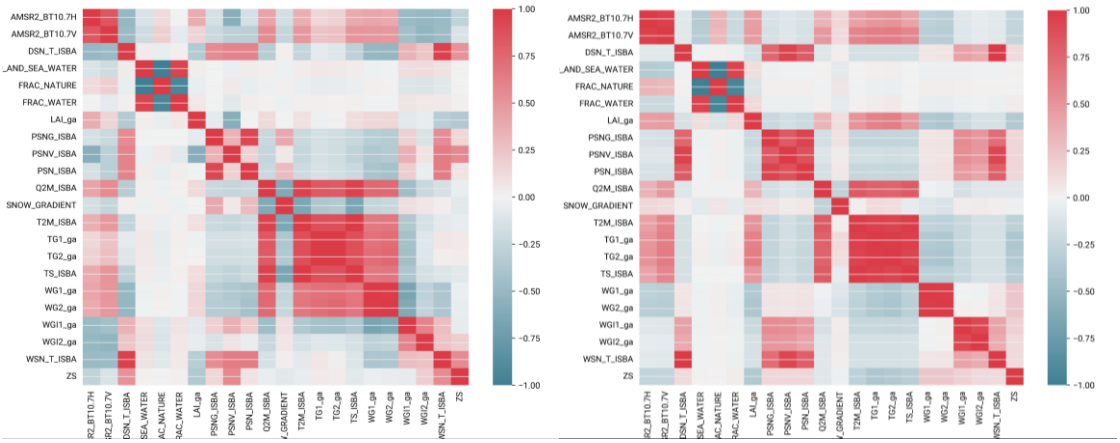

Figure 20: *Correlation heatmap between ISBA LSVs and AMSR2 18GHz V and H-polarization (top) and 10GHz V and H-polarization (bottom). The time-period is March, April and May 2018 (left) and June, July and August (right).*

Figure 20 shows aggregated statistics in time and space between the ISBA LSVs and AMSR2 18GHz (top) and 10GHz (bottom) for MAM (left) and JJA (right). For both 18GHz and 10GHz we note the positive correlation between surface soil moisture (WG1 and 2) for the MAM period. This is contradicting the microwave theory which has the inverse relationship. The expected negative correlation is seen for the JJA period. We also see that there is a negative correlation between snow depth/SWE and brightness temperature (Tb); this is higher for the 18GHz channel than the 10GHz channel.

We also see a high negative correlation between soil ice (WGI) and Tb, also more pronounced for 18GHz during MAM than for 10GHz. Finally, we note that there is a strong positive correlation between soil temperature variables and Tb.

Temporal correlations for the 18GHz channel are shown in Fig 21. Top panels show the correlation between snow depth and Tb for DJF (left) and MAM (right). We see that in the snow accumulation phase this correlation is negative in large parts of the domain, however at the Kola peninsula it is positive. For the MAM case the relationship is stronger (R=-0.6), and more homogeneous, except for sampling noise in the northern part of the domain. Regions with strong topography and glaciers are filtered out in this figure. Leaf area index (LAI) and soil temperature layer 1 correlations with Tb for JJA are plotted in the bottom panel. Here we see a positive correlation for both variables and it is particularly strong for soil temperature.

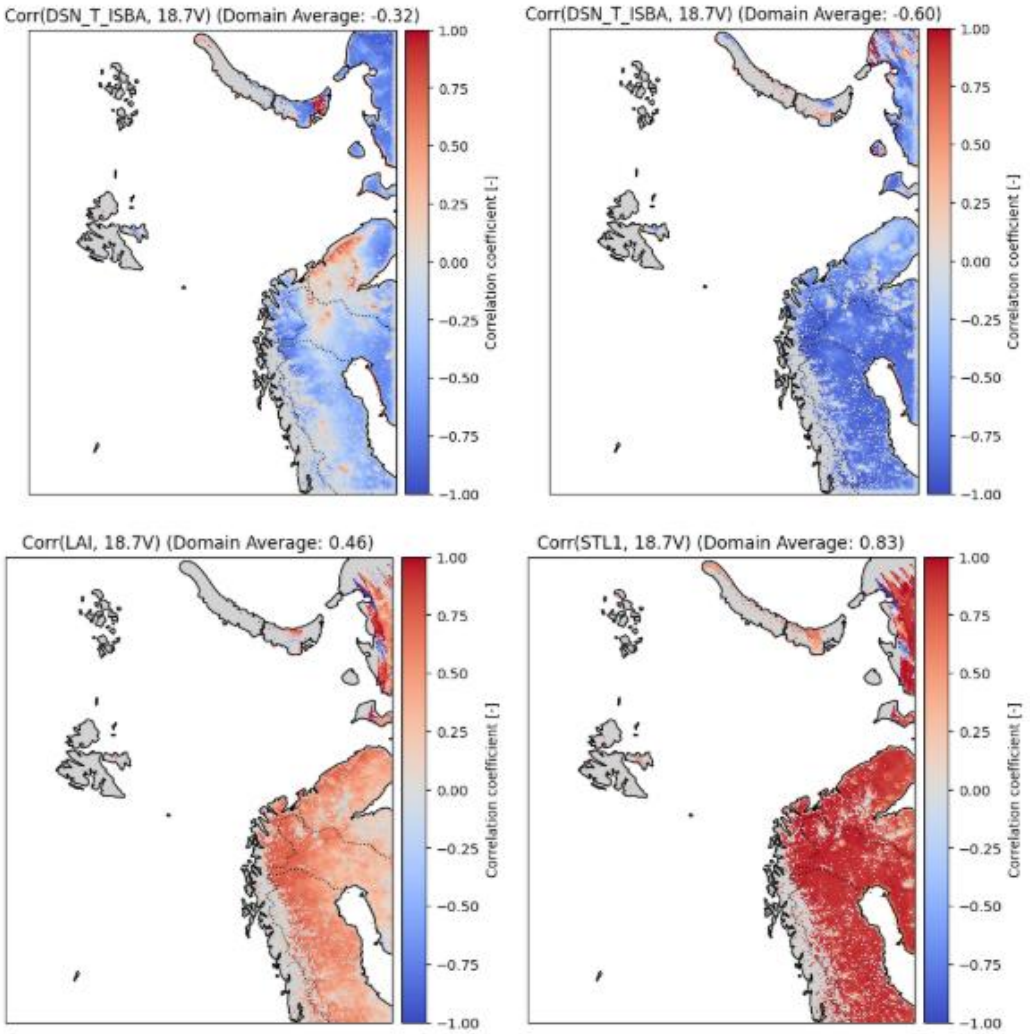

Figure 21: *Temporal correlation between snow depth (DSN_T_ISBA) and 18.7 GHz V-pol, top left) and top right) for DJF and MAM, respectively. lower left) temporal correlation between LAI and 18.7 GHz V-pol for JJA and lower right) temporal correlation between soil temperature layer 1 and 18.7 GHz V-pol for JJA.*

4.2.4 Forward modelling of passive microwave observations

In this section we present the forward modelling of passive microwave observations. We describe the different machine learning algorithms that were tested and the physics-based Community Microwave Emission Model (CMEM).

Machine learning forward operators

We investigated different flavours of machine learning algorithms, each with their own strengths and weaknesses. Here we briefly describe the different algorithms and their implementation.

First, we tested the XGBoost (eXtreme Gradient Boosting) algorithm, this model is based on decision trees that are updated in the training phase. In this model each grid point was considered a separate sample and there was no spatial context supplied to the model i.e., it is not able to explicitly represent the AMSR2 footprint. Our XGBoost is trained separately for different target variables.

Second, we implemented a footprint CNN (convolutional neural network) Yamashita, R. et al. (2018). It was developed for patches of 5 x 5 grid points. Thus it is able to learn spatial features within the patches. Here we make one prediction for each patch (the target is the mean observed value in a patch).

Third, we implemented a Residual U-net, here a CNN is developed for the full domain, and it is able to learn spatial features at different spatial scales (here 6 ranging from 7.5 to 240 km). It creates one prediction for each grid point and the model predicts all target variables. The downside with this model is that it is domain dependent.

Fourth we developed a graph neural network (GNN). In the GNN each graph has a set of nodes. Each node corresponds to an AMSR2 observation. Within the footprint area each node has a selected number of features, e.g. the ISBA LSVs grid points, see Fig 22. The area of the footprint is frequency dependent, thus is also the number of features for each frequency, see Fig. 20. We utilize a static number of grid points for each individual frequency, hence the GNN is said to be a static-GNN. The number of grid points for each frequency is listed in Table 3. We also tested a GNN where the number of nodes within the swath was allowed to vary. This is because the observations at the edge of a swath have a larger footprint than the observations close to the center, hence the number of ISBA grid points within a footprint is larger at the edge than at the center of the swath. This dynamic (varying nodes) was tested and found to give better results than the static-GNN (not shown). The computational cost of training the static-GNN was lower than for the dynamic-GNN and summary scores did not suffer too much when keeping the number of nodes static. The static-GNN is evaluated separately in Sec. 3.1.1.

Table 4: *Model settings for the different machine learning algorithms tested in this work.*

Model	Model or obs space	Training time	Training period	Validation period
XGBoost	Model	40 min	01-09-2020 to 01-05-2022	01-09-2022 to 01-06-2023
footprint CNN	Model	2 hours	01-09-2020 to 01-05-2022	01-09-2022 to 01-06-2023
Residual U-Net	Model	8 hours	01-09-2020 to 01-05-2022	01-09-2022 to 01-06-2023
static-GNN	Observation	24 hours for 18GHz channel	01-09-2020 to 01-05-2022	01-09-2022 to 01-06-2023

In Table 4 we show characteristics of the different machine learning algorithms. They all use the same training and validation dataset, however the training time differs from 40 min (XGBoost) to 24 hours (static-GNN).
The sensitivity analysis performed in Sec. 2.3 guides the selection of feature variables for the observation operator. The final set of variables are listed in Table 5.

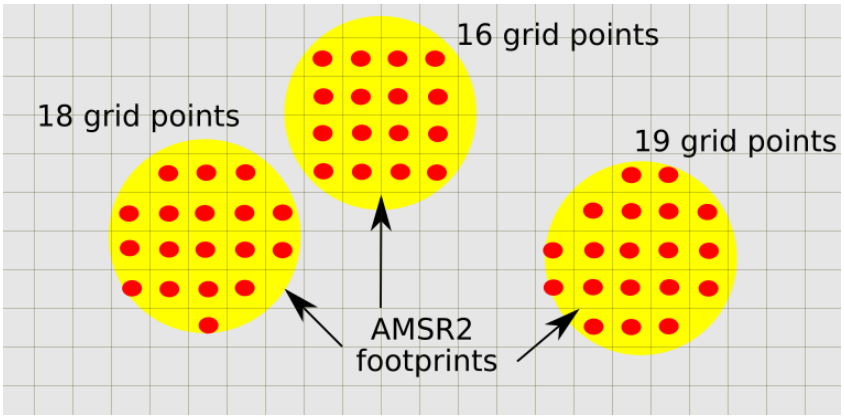

Figure 22: *Illustration of the dynamic/static graph neural network approach. AMSR2 footprint in yellow and the corresponding ISBA LSV grid points selected for that node.*

Table 5: *List of ISBA LSV variables that we use in the static-GNN.*

Geophysical parameters			
Static	**Snow**	**Soil**	**Vegetation**
ZS	Depth	Temperature	LAI
Patch fraction	Density	Moisture	-
Fraction of land and sea	SWE	Ice	-
Distance to footprint center	Liquid water	-	-
-	Heat content	-	-
-	Temperature	-	-

Implementation in Harmonie-Arome

The static-GNN is implemented in both the offline reanalysis system (CARRA-Land-Pv2) and in the coupled regional demonstrator (CARRA3-Pv1). For both systems the static-GNN is trained on one year of open-loop data covering the pan-Arctic domain (spinup for CARRA-Land-Pv2). For training we utilize the 20 last days of the month (for every month) as training dataset and the first 10 days (of every month) for validation.
Figure 23 shows the setup in the coupled system, here the MakeObsOpData task takes the FA (native Harmonie-Arome filetype) input and converts ISBA LSVs and observations into a graph for the static-GNN, which is then run for each ensemble member in the sfc_obsOp task. The LETKF (see D1.3) is extended to assimilate AMSR2 Tb in 10.7, 18.7 and 36.5 GHz V and H-pol.

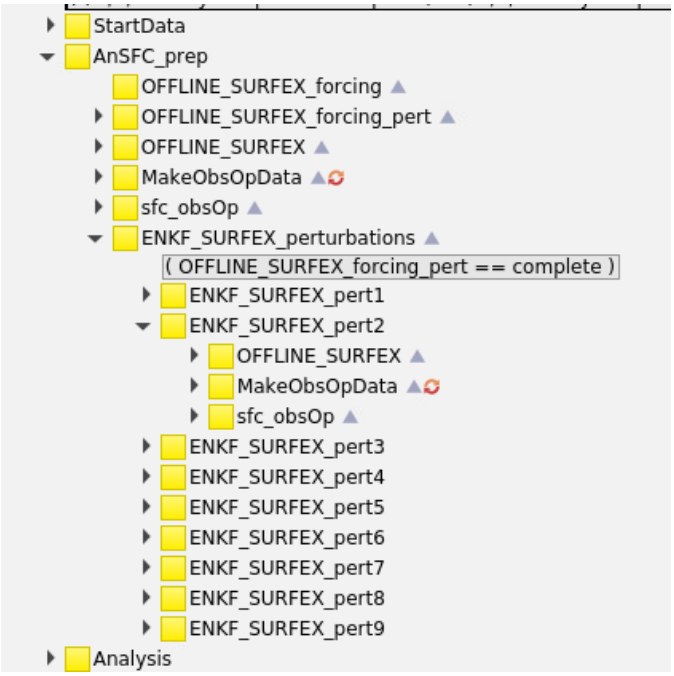

Figure 23: *Ecflow graphics of the static-GNN implemented in Harmonie-Arome. The MakeObsOpData task takes the FA (native Harmonie-Arome filetype) input and converts SURFEX variables and observations into a graph for the static-GNN which is then run for each ensemble member in the sfc_obsOp task*

Community microwave emission model (CMEM)

The Community Microwave Emission Model (CMEM) is developed and maintained by ECMWF. It is a forward operator for low frequency microwave observations, see de Rosnay et al. (2019). CMEM has a modular structure for computing the microwave emission contributions from soil, vegetation, snow and the atmosphere. The code is designed to be highly modular and for each microwave modeling component, a choice of several parameterizations is considered, see https://confluence.ecmwf.int/display/LDAS/CMEM+Documentation. We use CMEM as a baseline to evaluate the static-GNN for the 10GHz channel. To ensure a fair comparison between CMEM and the static-GNN we run CMEM on graph level, i.e., for each node we compute the footprint average value of the ISBA LSV inputs. In this way we run CMEM in "observation" space as we do for the static-GNN. For the different module and parameterization options we follow Hirahara et. al (2020) as close as possible. The selected options are listed in Table 6.

Table 6: *List of parameterizations utilized in CMEM*

CMEM module	**Parameterization**
Soil dielectric mixing	Dobson
Effective temperature	Chodhury
Soil roughness	Wegmuller
Vegetation optical depth	Wegmuller
Vegetation temperature	Dual
Vegetation dielectric mixing	Matzler

Vegetation dielectric mixing (cold)	Not frozen
Snow emission model	HUT single layer
Soil volumetric moisture	Input ISBA LSVs
Atmospheric emission model	Ulaby

4.3 Results

In this section we present an evaluation of the different machine learning algorithms, a closer look at the dynamic vs static-GNN and a comparison of the static-GNN vs CMEM.

4.3.1 Evaluation of the different machine learning algorithms

To allow for rapid prototyping and testing of different machine learning algorithms we chose a relatively small domain covering southern parts of Norway and western Sweden, see Fig. 24. The topography in this domain ranges from steep mountains to flat forested and agricultural areas. It also has a strong seasonal cycle with a domain average number of days with snow cover larger than 0.5 reaching 106.3 during the whole training/validation period.

In Fig. 25 we plot predicted brightness temperature at 36.5 GHz V-pol at 18-03-2023 for XGBoost, footprint CNN (with stride 5), footprint CNN (with stride 1), Residual U-Net and the observed brightness temperature. We see that topography (and most likely snow cover and frozen land) are strong predictors of AMSR2 brightness temperature. We also note that the Residual U-Net is capturing the high brightness temperature close to the Norwegian/Swedish border. The Residual U-Net's ability to learn spatial features at different spatial scales also improves the qualitative match between the prediction and the observation, in particular when compared to XGBoost which only has information at the grid point scale.

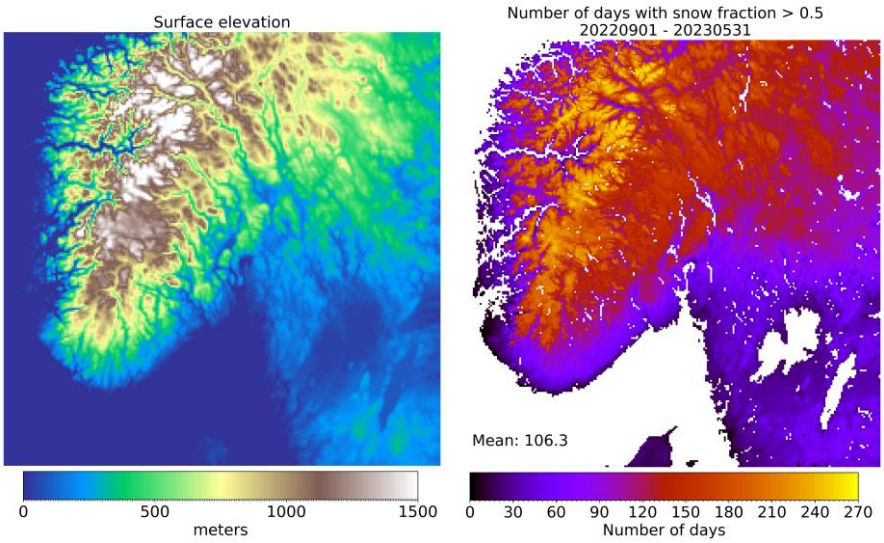

Figure 24: *Illustration of domain characteristics for the dataset used in training the machine learning observation operators. (Left) Surface elevation in meters, (right) number of days with snow fraction > 0.5 in the dataset.*

A more comprehensive analysis is shown in Fig. 26, where we plot the domain averaged mean absolute error (MAE) for channel 18.7 GHz V-pol for the whole validation period and for

different seasons, SON, DJF and MAM. Overall, the XGBoost (blue) has a larger MAE than the more complex methods, with the Residual U-Net showing the smallest MAE throughout the time-period. When we look more closely at the different seasons we see that the errors are smallest during fall (SON) and increasing into DJF (most likely because of snow accumulation). Here the differences between the models are smaller and towards the melting season (MAM) they overlap to a larger extent. The errors are also fluctuating more, this could be because of freeze/melt cycles in the snow pack during spring.

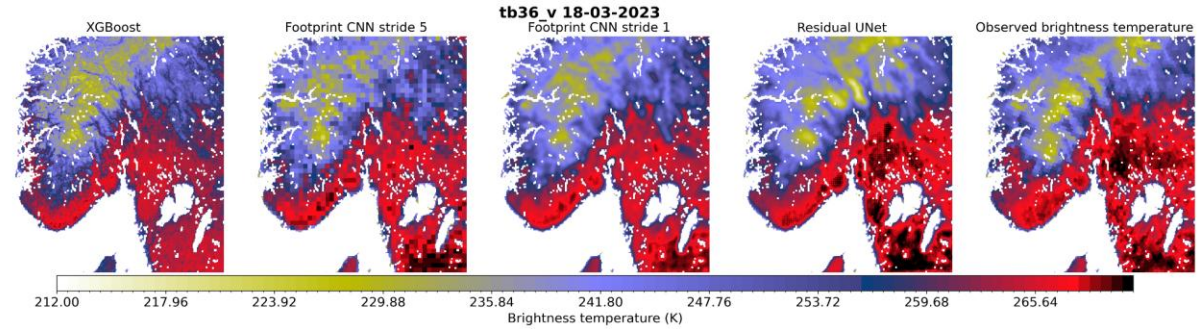

Figure 25: *Comparison of predicted brightness temperature at 36.5 GHz V-pol at 18-03-2023 for XGBoost, footprint CNN (with stride 5), footprint CNN (with stride 1), Residual U-Net and the observed brightness temperature.*

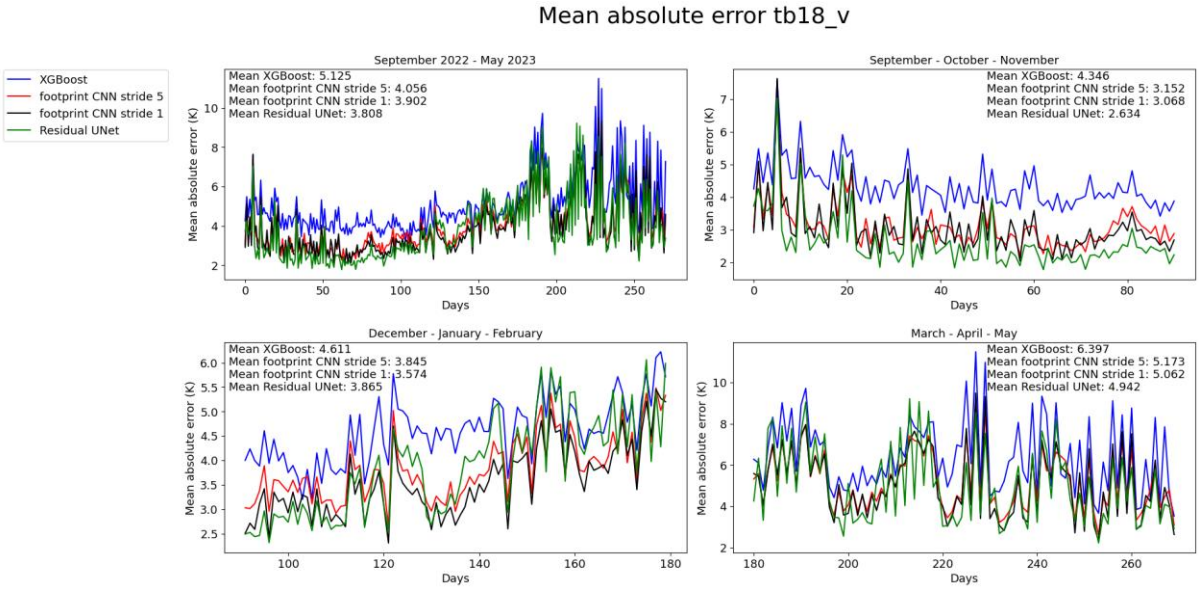

Figure 26: *Domain average mean absolute error (MAE) for channel 18.7 GHz V-pol, for the different machine learning algorithms and seasons. XGBoost (blue), footprint CNN with stride 5 (red), footprint CNN with stride 1 (grey) and the Residual U-Net (green). Shown are the whole period of September 2022 to May 2023 (top left) and 3-month windows SON (top right), DJF (bottom left) and MAM (bottom right).*

Figure 27 shows the spatial distribution of the errors. For 18GHz V-pol (top) we see that increased model complexity reduces the domain mean MAE. Smallest MAE are seen in flat regions with fewer days with snow cover (Sweden), but also in northern regions of south Norway and along the southern coast of Norway. In general the MAE is larger for the 36GHz V-pol (bottom). One plausible explanation for this could be the lack of atmospheric predictors in our feature list.

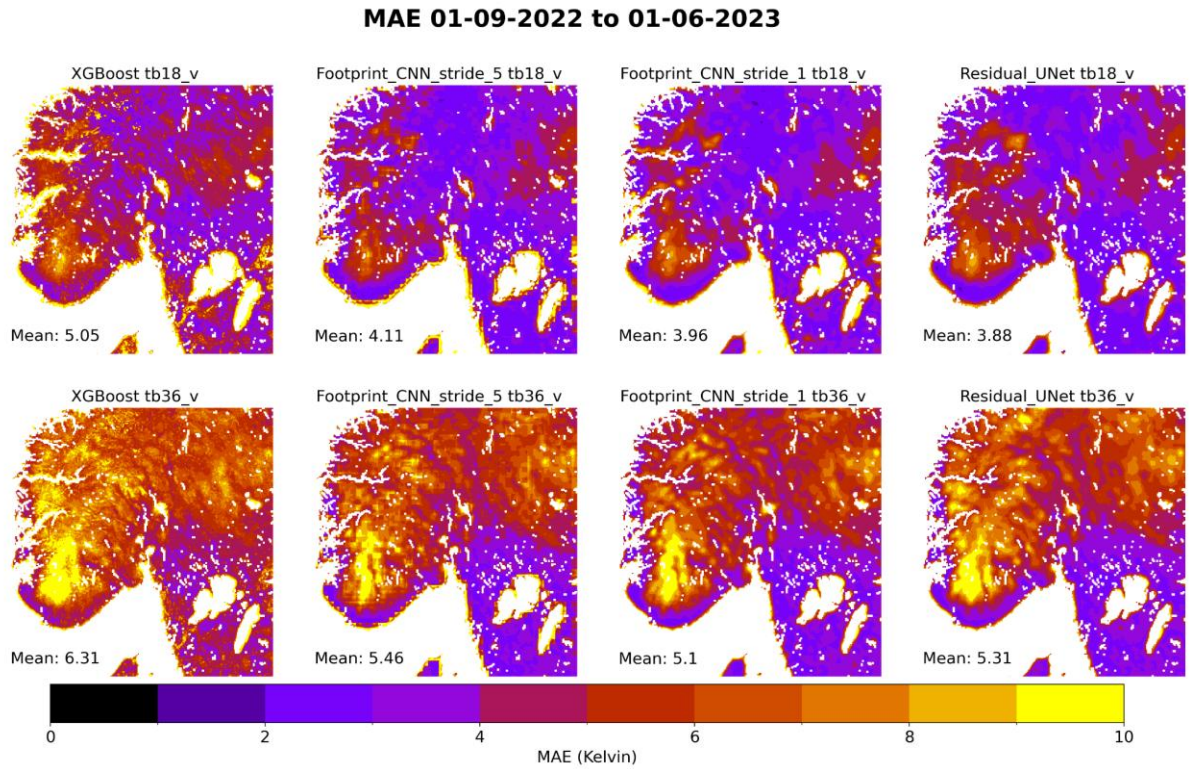

Figure 27: *Time averaged mean absolute error (MAE) for the different machine learning algorithms. Top 18.7 GHz V-pol and bottom 36.7 GHz V-pol.*

For the 36GHz channel the smaller MAE are seen along the coast of south Norway and in the flat agricultural dominated regions of Sweden (compared to more forest to the north). Errors are particularly large inland in south Norway, without any clear explanation from topography or number of snow covered days (e.g. not glacier).

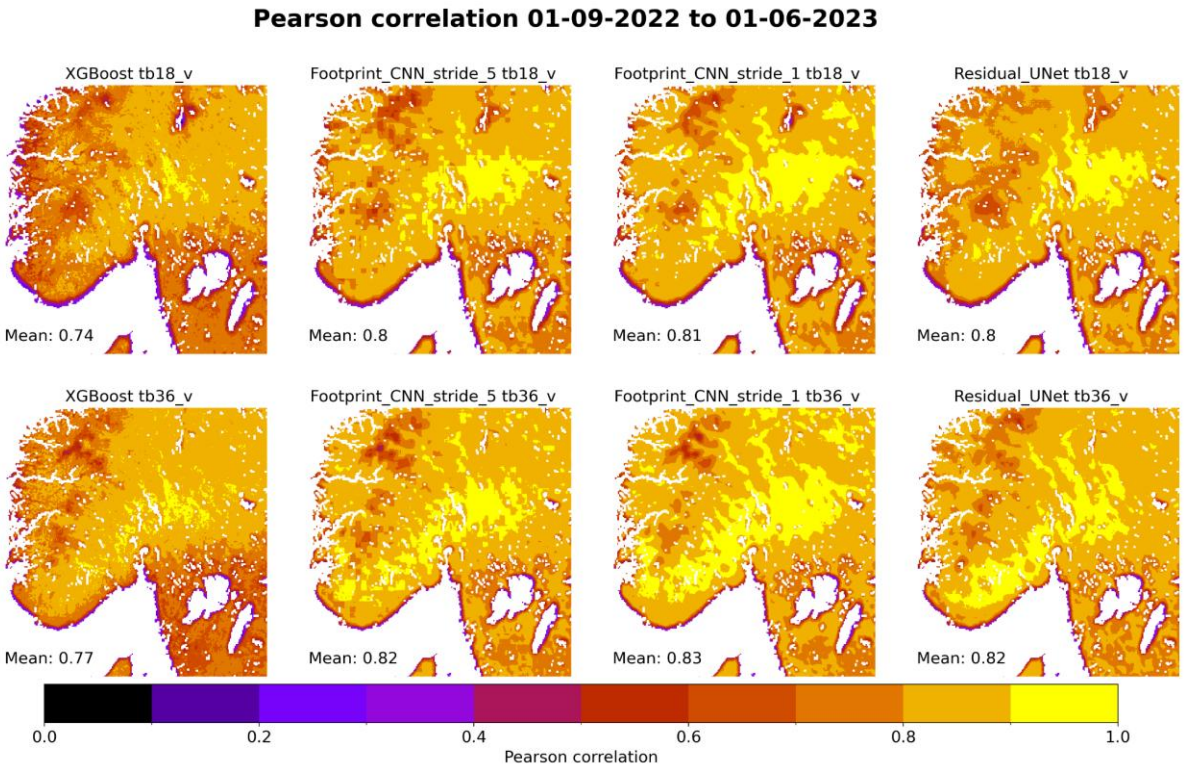

Figure 28: *Pearson correlation coefficient for the different machine learning algorithms. Top 18.7 GHz V-pol and bottom 36.7 GHz V-pol.*

Maps of temporal correlation, Fig. 28, show that there are small differences between the more complex models, and that the XGBoost has a much smaller correlation than the other models. Red regions in western Norway (with low correlation) are regions with permanent snow (glaciers), especially Jostedalsbreen and Folgefonna. A reason for the lower correlation in these regions could be because the land surface model does not represent the glacier as ice with snow on top, but as a very deep snowpack. The feature variables of the model are therefore not able to capture the variability of the observed brightness temperature.

4.3.2 Dynamic vs static graph neural network

As described above we developed two flavours of the GNN, one dynamic (with varying number of grid points for each node) and one static (with static number of grid points for each node). While the dynamic-GNN is an attractive approach, as it is able to take into account the varying spatial footprint of the AMSR2 instrument within a swath (larger closer to the edge vs at nadir), it was found to be computationally expensive. Figures 29 and 30 show bias, MAE, root-mean-squared-error (RMSE) and correlation for the dynamic and static-GNN, respectively. Overall the largest differences in scores are seen for bias.

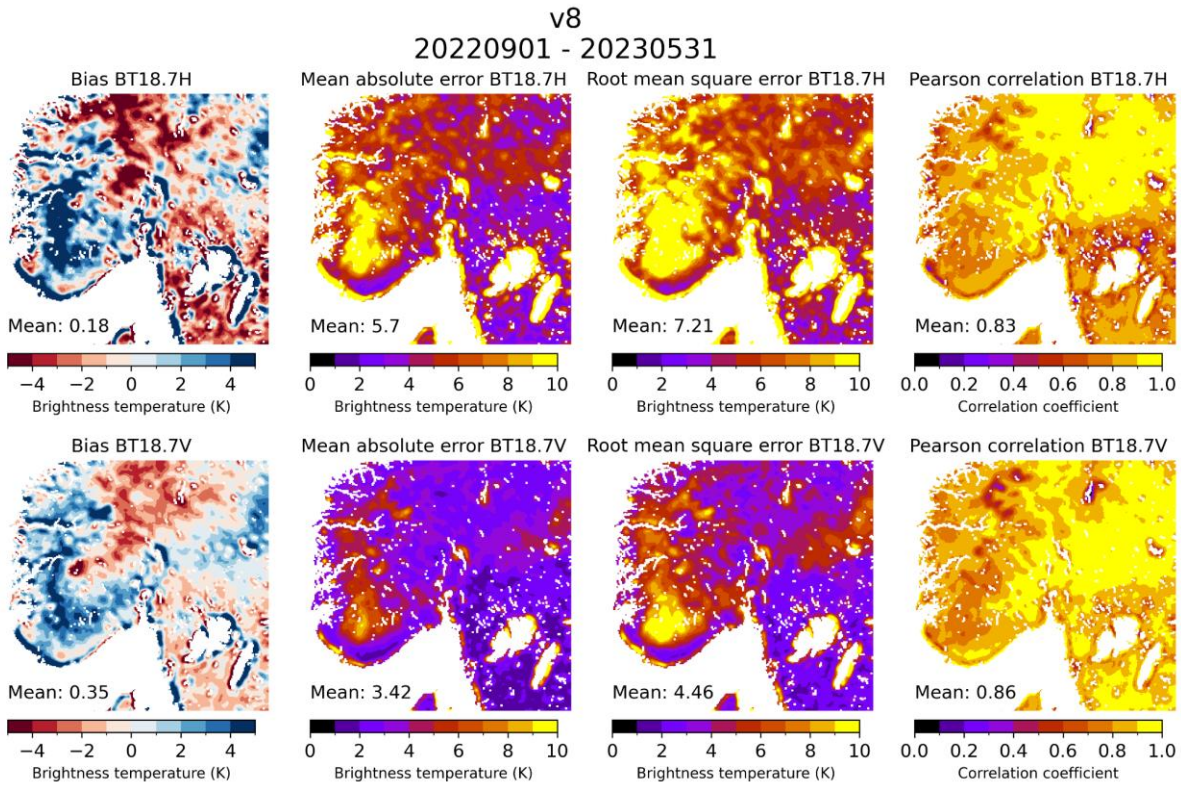

Figure 29: *Bias, MAE, RMSE and correlation for the dynamic graph neural network, top 18.7 GHz H-pol and bottom 18.7 GHz V-pol.*

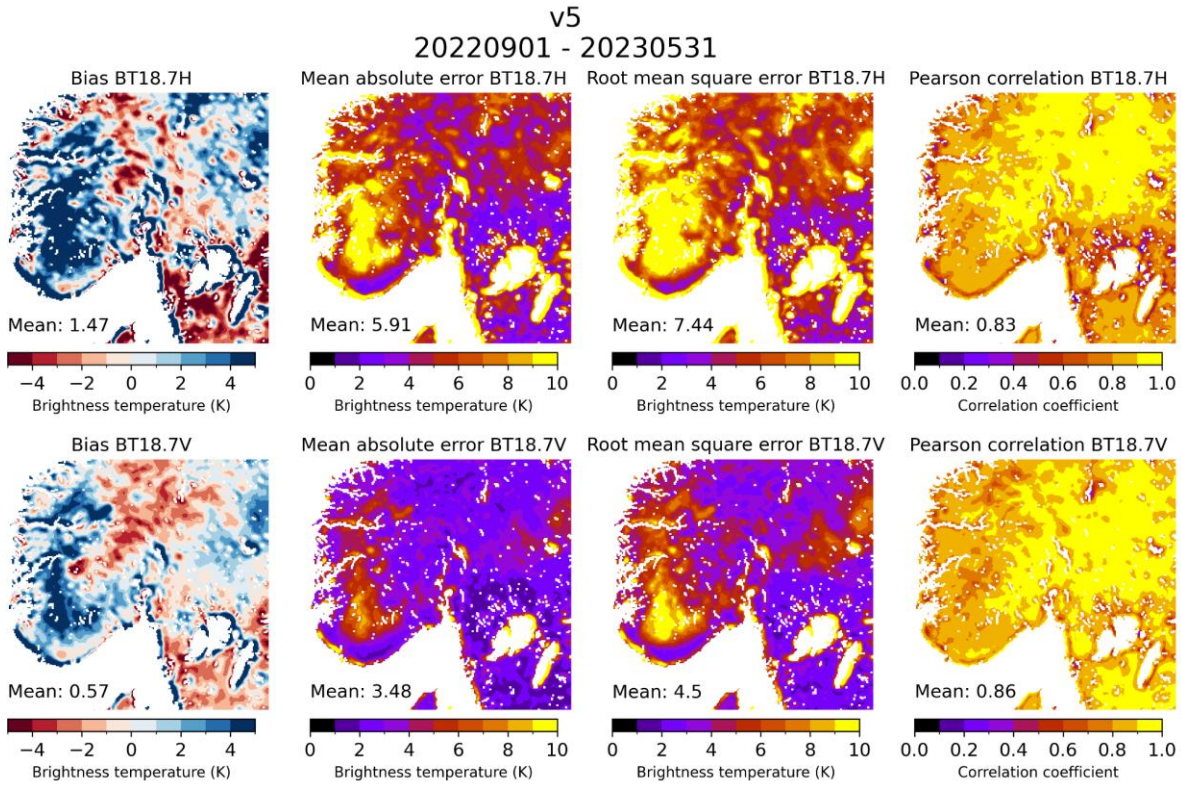

Figure 30: *Bias, MAE, RMSE and correlation for the static graph neural network, top 18.7 GHz H-pol and bottom 18.7 GHz V-pol.*

4.3.3 Training and evaluation of the static-GNN over the CARRA East domain

We further evaluate the static-GNN by training it over the CARRA East domain. This is a larger domain situated in the European Arctic. We use the same training strategy as outlined in Sec 2.4.2. A comparison is made between the static-GNN and CMEM for an independent validation dataset covering 4th June 2018 until 14th August 2018. We compute mean bias and MAE for this time-period in observation space. By construction the ML-methods should have a long-term zero bias. This is seen for the static-GNN, although with some large positive bias in the northern parts of the domain (most likely because of few observations). Bias in CMEM is larger, and there is usually a need for a priori bias correction when utilizing physics based models as forward operator. Looking into the MAE (Fig. 31 right), we see that the static-GNN has a lower domain average MAE ~5.25 K vs ~7.76 for CMEM. The static-GNN shows particularly low MAE for inland mainland Norway.

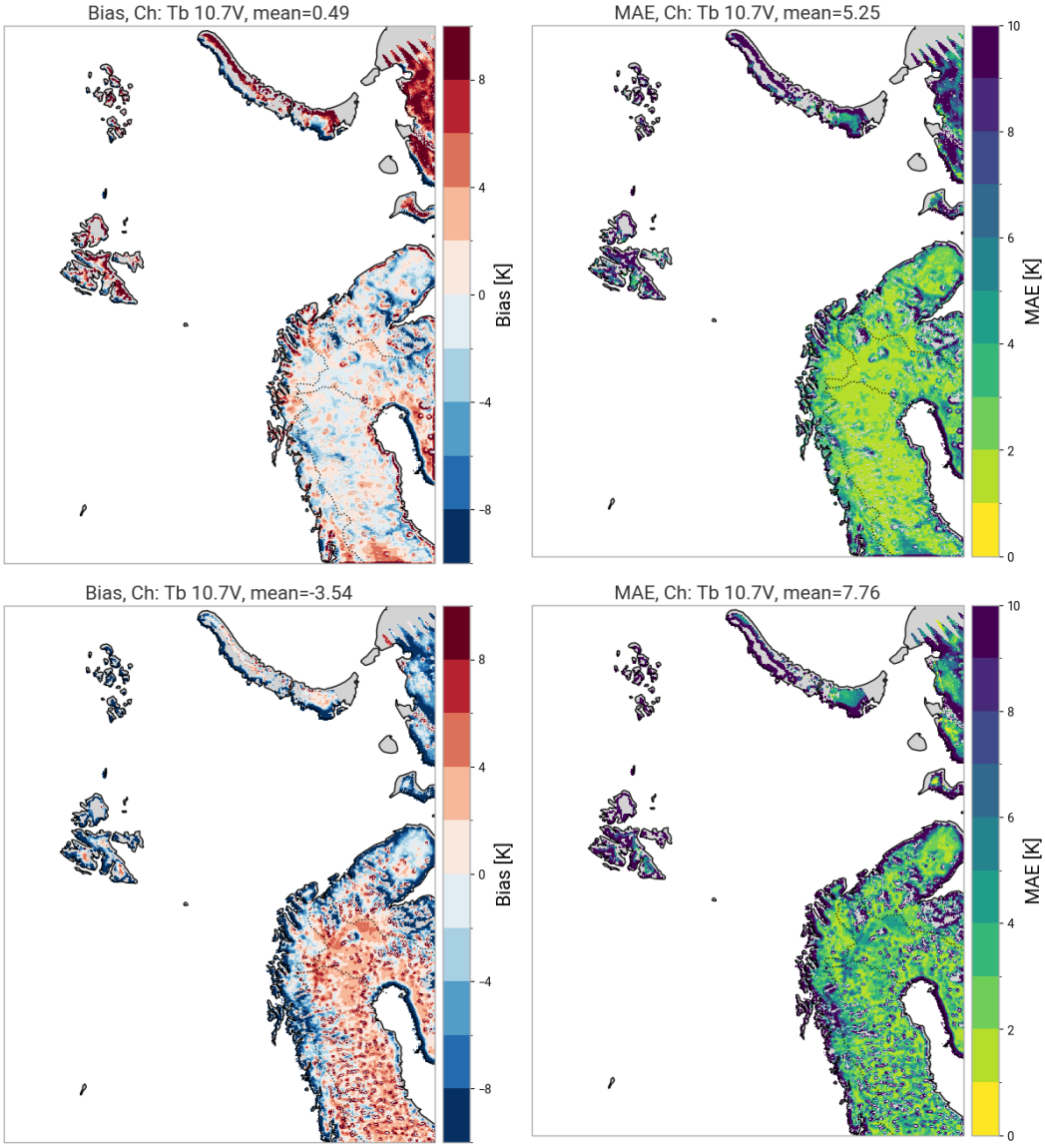

Figure 31: *(Top left) Bias between observed 10GHz V-pol and static-GNN predicted for the time-period 04-06-2018 to 14-08-2018. (Top right) Mean absolute error (MAE) for the same time-period. (Bottom left) same as top left but for CMEM, (bottom right) as top right but for CMEM.*

4.4 Conclusion

In this Section we have described the implementation and testing of different machine learning algorithms for usage in both the offline and coupled reanalysis systems. We developed a static graph neural network (static-GNN) that was able to account for the spatial heterogeneity of the land surface model within a satellite footprint. Preliminary analysis shows that the static-GNN model is able to outperform the physics-based CMEM which is promising for use in land data assimilation. The next step will be to evaluate the static-GNN for usage in an ensemble data assimilation system.

5. ML-based observation operator for hydrological applications

In this report we present the development of a machine-learning-based observation operator for assimilation of passive microwave data using data from AMSR2 sensor, land surface variables and a gradient boosting regressor method.

5.1 Data and Methods

A dataset consisting of AMSR2 brightness temperatures, Tb, at daily time step and 10 km spatial resolution was compiled for the period 2019-2023 (Japan Aerospace Exploration Agency, 2012) for northern Sweden. The study area covers 154,700 km², extending from the mountains along the border with Norway to the Baltic Sea (Figure 32). The mean elevation is 418 meters above sea level, and the landscape is predominantly characterized by forests and open lands. The area includes the basins of two major rivers in northern Sweden, the Umeälven and the Tornälven rivers.

The semi-distributed hydrological HYPE model (Lindström et al., 2010) was used to generate the land surface variables. The model was set up on a grid of 0.05x0.05 degrees to create an interface with satellite products. To consider the influence of the surface data sub-grid variability, we considered their values associated with the different land cover classes within the AMRS2 pixels. We selected surface variables including snow depth, snow temperature and liquid water content, frost depth, soil moisture and upper soil layer temperature (Table 7). In addition, we considered the static variables of land cover fractions and spatial coordinates as input features (Table 7). The four-year dataset was temporally split into training (2019-2021) and testing (2022-2023) sets.

Figure 32: *The map of the study area in northern Sweden with the main land cover types*

Table 7: *List of the variables, target, and input features used for the development of the observational operator.*

	Variable	Acronym
Target	Brightness temperature	Tb
Input features	Snow depth	sdep
	Snow surface temperature	Tss
	Snow liquid water content	lwcs
	Frost depth	fdep
	Soil moisture fraction	smf
	Upper soil / lake temperature	Tusoil, Tlake
	Land cover fractions	Fract
	Xcoor, Ycoord	xcoord, ycoord

We trained an eXtreme Gradient Boosting Regression (XGBoost) with the time-series of surface variables and the static land cover fractions and spatial coordinates to predict Tb at 18GHz. The eXtreme gradient Boosting Regressor was selected for the capabilities in modelling complex non-linear relationships and variable interactions. Boosting is an ensemble method that constructs ensemble members sequentially. Here, the ensemble members are decision trees that iteratively split the input features to predict the target variable. In boosting, the splits are modified in each iteration to put more emphasis on the data points for which the model so far has performed poorly. The algorithm minimizes the loss function by finding the direction in which the loss function decreases the fastest (Lindholm et al., 2022).

The optimal parameters were found using the GridSearchCV cross-validation technique with a step-wise approach, minimizing the mean squared error score function. The mean absolute error (mae) and the root mean squared error (rmse) between observed and predicted Tb were calculated pixel-wise over the whole spatial domain to evaluate the model performance over the year and at the seasonal time scale in winter (November-March) and summer (June-August) of 2022-2023.

5.2 Results

5.2.1 Data exploration

We calculated Pearson's correlations between the brightness temperature data and the input features for the whole datasets (Figure 33). The highest negative correlations were found between brightness temperature (Tb) and snow depth of the forest open and lake classes. The highest positive correlations were found between brightness temperature (Tb) and the upper soil temperature of the forest (Tusoil) and the water temperature of the lake classes (Tl). Some collinearities were found among the input features such as forest fraction with open fraction and forest soil moisture fraction or lake temperature and upper soil temperature of the forest class. However, the gradient boosting regression algorithm shows small sensitivity to collinearity and all the features were considered.

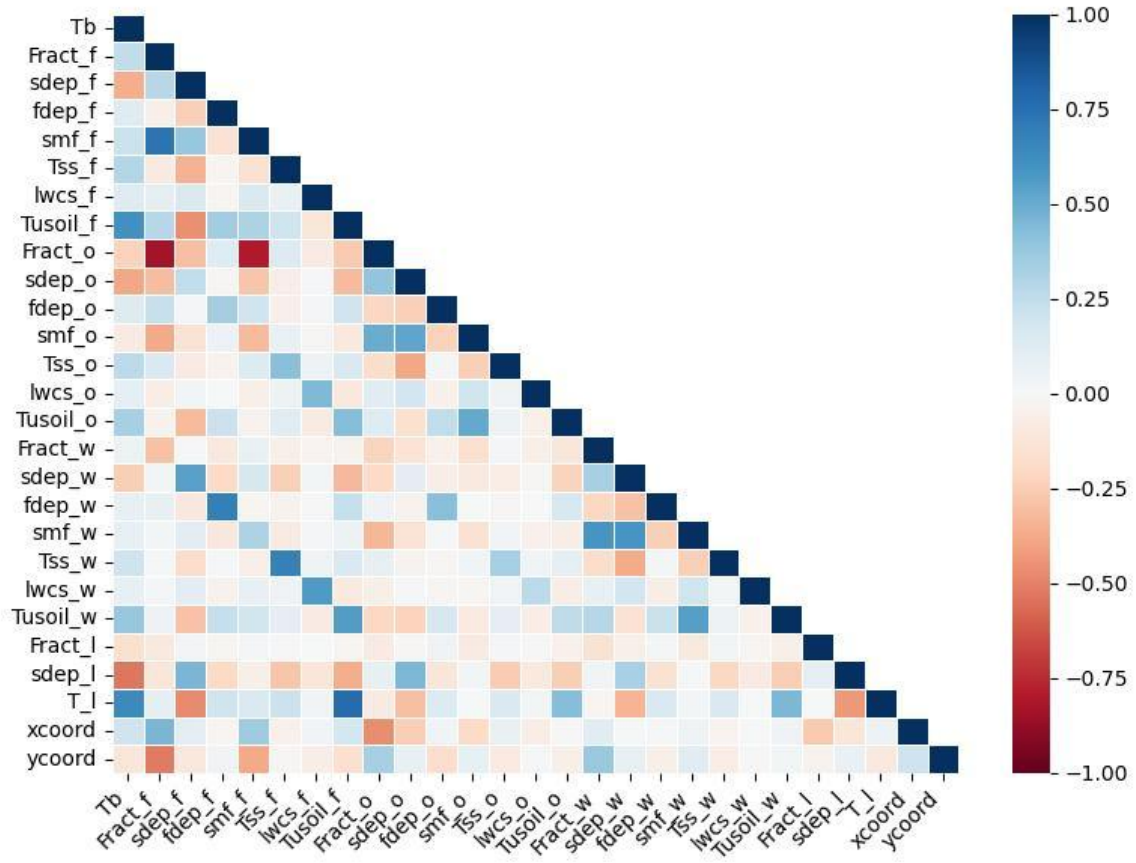

Figure 33: *Pearson's correlation matrix of the target (Tb) and the 11 input features (Table 7) for each land cover class, forest (f), open (o), wetlands (w) and lake (l) calculated over the entire dataset.*

5.2.2 Model evaluation

The evaluation of the model showed that it generally captured the Tb spatial variability well (Figure 34). The mean absolute error averaged around 4 K over the year, 5 K in winter and 3 K in summer (Figure 34). High error occurred in a few pixels along the coast during winter, where the observed brightness temperatures are significantly lower than those in neighboring areas and are likely affected by the sea microwave emissions. The largest differences were observed in winter in the inland forested areas, whereas a better agreement between observations and predictions was found in the mountainous region above the tree line. This result could be due to a winter snow season in the testing dataset that differs significantly from that in the training dataset or due to a limitation of the HYPE model in capturing the snow dynamics in forested areas. The smallest differences were found in summer across the whole domain. The root mean squared error was slightly higher than the mean absolute error, but it showed similar spatial patterns.

Next steps include analyzing the impact of each surface variable on Tb predictions to understand the spatial differences in the ML-based observation operator performance we observed. The Python-based observation operator will be further implemented in the HYPE model data assimilation module using libraries for Fortran-Python interoperability. Assimilation of AMSR2 brightness temperatures using the operator will be tested and evaluated as part of the Arctic-HYPE pan-arctic hydrological re-analysis during 2026.

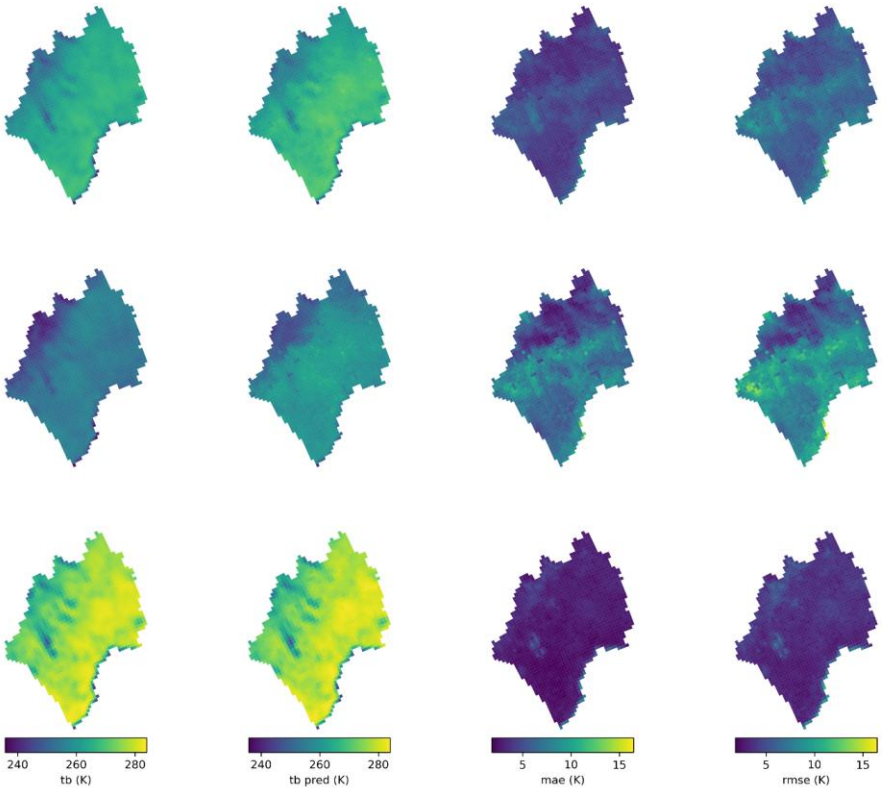

Figure 34: *Map with the observed (tb), predicted brightness temperature (tb pred) at 18GHz, mean absolute error (mae) and root mean squared error (rmse) between observed and predicted tb for annual (upper), winter (middle) and summer (lower) 2022-2023 period in northern Sweden.*

6. Conclusion and next steps

The ML-based observation operators to estimate microwave emissivities, for both global and regional land data assimilation systems, have been developed using innovative methods and with the most advanced training data available. They have been thoroughly evaluated and compared to existing baseline models based on climatologies and physics-based models. The initial results suggest that the ML-based models are able to outperform the existing models. Their quality and limitations are thoroughly illustrated to help their forthcoming use in assimilation or other contexts.

The next steps are to test the models in land and coupled data assimilation experiments in the IFS and HARMONIE-AROME. Since many developments have been conducted in this work package, perspectives are numerous. In particular, some ideas could be used to reconcile the advantages of regional models (specialization over a particular domain with specificities) and a global approach (able to be used easily in the assimilation scheme). Other perspectives could be the estimation of the uncertainties of the model (a feature that is available in TELSEM climatology).

7. Annex I: Codes for the ML-based observation operator for use in a global coupled assimilation system

7.1. The code: SURFEM-Snow

The forward model for continental snow package is mainly composed of two MATLAB scripts and a folder containing resources for the modeling.

1) forward_model_continental_snow.m: This is the main script of the proposed forward model. This script implements the emissivity retrieval for continental snow.

2) test_forward_model_snow.m: This script provides examples on how to run the precedent script, and tests with different configurations.

3) Resources_snow: This folder contains necessary resources to run forward_model_ continental_snow.m. In particular, climatologies of emissivity are used in the process to retrieve emissivity whether for the dynamic emissivity computation or directly for permanent glacier (e.g., Greenland or Antarctica) where geophysical parameters required for a dynamic computation are not available. These climatologies are provided in Resources_snow folder. It also contains flags to indicate where permanent glaciers are. Finally, it includes the Above Ground Biomass coming from the European Space Agency (ESA) Climate Change Initiative (CCI) averaged over 2018 and 2019 (Santoro et al., 2023).

7.2. The code: SURFEM-Land

The forward model for land package is mainly composed of two MATLAB scripts and a folder containing resources for the modeling.

1) forward_model_land.m: This is the main script of the proposed forward model. This script implements the emissivity retrieval for land not covered with snow.

2) test_forward_land.m: This script provides examples on how to run the precedent script, and tests with different configurations.

3) Resources_land: This folder contains necessary resources to run forward_model_ land.m. In particular, climatologies of emissivity are used in the process to retrieve emissivity. These climatologies are provided in Resources_land folder. Finally, it includes the Above Ground Biomass coming from the European Space Agency (ESA) Climate Change Initiative (CCI)

averaged over 2018 and 2019 (Santoro et al., 2023), the permanent water from GLWD-v2 (Lehner et al., 2025) and the climatology of open surface water presence computed from GIEMS-2 (Prigent et al., 2020).

8. References

Al Bitar, A., Mialon, A., Kerr, Y. H., Cabot, F., Richaume, P., Jacquette, E., et al. (2017). The global smos level 3 daily soil moisture and brightness temperature maps. Earth System Science Data, 9(1), 293–315. https://doi.org/10.5194/essd-9-293-2017

Albergel, C. et al. Sequential assimilation of satellite-derived vegetation and soil moisture products using SURFEX-v8.0: LDAS-Monde assessment over the Euro-Mediterranean area. Geosci. Model Dev. 2017, 10, 3889–3912.

Baordo, F., Geer, A. (2016). Assimilation of SSMIS humidity-sounding channels in all-sky conditions over land using a dynamic emissivity retrieval. Q. J. R. Meteorol. Soc. 142, 2854–2866. http://dx.doi.org/10.1002/qj.2873.

Blyverket et al., Manuscript in prep: Microwave observation operator for the land surface using static Graph Neural Networks (2025).

Boone, A., et al., The interactions between soil–biosphere–atmosphere land surface model with a multi-energy balance (ISBA-MEB) option in SURFEXv8 – Part 1: Model description, Geoscientific Model Development, 10, 843–872, https://doi.org/10.5194/gmd-10-843-2017, publisher: Copernicus GmbH, 2017.

Bormann, N., Lupu, C., Geer, A., Lawrence, H., Weston, P., English, S. (2017). Assessment of the Forecast Impact of Surface-Sensitive Microwave Radiances Over Land and Sea-Ice. European Centre for Medium Range Weather Forecasts.

Brodzik, M.J., Billingsley, B., Haran, T., Raup, B., Savoie, M.H., 2012. EASE-grid 2.0: Incremental but significant improvements for Earth-gridded data sets. ISPRS Int. J. Geo. Inf. 1, 32–45. http://dx.doi.org/10.3390/ijgi1010032.

Cordisco, E., Prigent, C., Aires, F. (2006). Snow characterization at a global scale with passive microwave satellite observations. J. Geophys. Res.: Atmospheres 111, http://dx.doi.org/10.1029/2005JD006773.

de Gélis, I., Prigent, C., Jimenez, C., & Sandells, M. (2025). Forward modelling of passive microwave emissivities over snow-covered areas at continental scale. Remote Sensing of Environment, 328, 114821.

de Rosnay, P., Munoz-Sabater, J., Albergel, C., Isaksen, L., English, S., Drusch, M., & Wigneron, J. P. (2020). SMOS brightness temperature forward modelling and long term monitoring at ECMWF. Remote Sensing of Environment, 237, 111424. ISSN 0034-4257, https://doi.org/10.1016/j.rse.2019.111424.

de Rosnay, P., Browne, P., de Boisséson, E., Fairbairn, D., Hirahara, Y., Ochi, K., Schepers, D., Weston, P., Zuo, H., Alonso-Balmaseda, M., et al. (2022). Coupled data assimilation at ECMWF: Current status, challenges and future developments. Q. J. R. Meteorol. Soc. 148, 2672–2702. http://dx.doi.org/10.1029/1999JD900486.

Decharme, B., Boone, A., Delire, C., and Noilhan, J.: Local evaluation of the Interaction between Soil Biosphere Atmo-sphere soil multilayer diffusion scheme using four pedotransfer functions, Journal of Geophysical Research: Atmospheres, 116, https://doi.org/10.1029/2011JD016002, https://agupubs.onlinelibrary.wiley.com/doi/pdf/10.1029/2011JD016002, 2011.

Derksen, C., 2008. The contribution of AMSR-e 18.7 and 10.7 GHz measurements to improved boreal forest snow water equivalent retrievals. Remote Sens. Environ. 112, 2701–2710. http://dx.doi.org/10.1016/j.rse.2008.01.001.

English, S.J., (1999). Estimation of temperature and humidity profile information from microwave radiances over different surface types. J. Appl. Meteorol. Clim. 38, 1526–1541. http://dx.doi.org/10.1175/1520-0450(1999)038<1526:EOTAHP> 2.0.CO;2.

Entekhabi, D., Njoku, E. G., O'neill, P. E., Kellogg, K. H., Crow, W. T., Edelstein, W. N., et al. (2010). The soil moisture active passive (smap) mission. Proceedings of the IEEE, 98(5), 704–716. https://doi.org/10.1109/jproc.2010.2043918.

Favrichon, S., Prigent, C., Jimenez, C., & Vogt, R. (2023). Global mapping of microwave emissivity and emitting depth in arid areas using GMI observations. Earth and Space Science, 10(11), e2022EA002756. https://doi.org/10.1029/2022EA002756

Foresee, F.D., Hagan, M.T. (1997). Gauss-Newton approximation to Bayesian learning. In: Proceedings of International Conference on Neural Networks. ICNN'97, 3, IEEE, pp. 1930–1935. http://dx.doi.org/10.1109/ICNN.1997.614194.

Geer, A., Lonitz, K., Duncan, D., Bormann, N. (2022). Improved surface treatment for all-sky microwave observations. Tech. Memo. 894.

Grippa, M., Mognard, N., Le Toan, T., Josberger, E. (2004). Siberia snow depth climatology derived from SSM/I data using a combined dynamic and static algorithm. Remote Sens. Environ. 93, 30–41. http://dx.doi.org/10.1016/j.rse.2004.06.012.

Hersbach, H., Bell, B., Berrisford, P., Hirahara, S., Horányi, A., Muñoz-Sabater, J., Nicolas, J., Peubey, C., Radu, R., Schepers, D., et al. (2020). The ERA5 global reanalysis. Q. J. R. Meteorol. Soc. 146, 1999–2049. http://dx.doi.org/10.1002/qj. 3803.

Hirahara, Y., Rosnay, P.d., Arduini, G. (2020). Evaluation of a microwave emissivity module for snow covered area with CMEM in the ECMWF integrated forecasting system. Remote. Sens. 12, 2946. http://dx.doi.org/10.3390/rs12182946.

JAXA. (2013). Gcom, w1 shizuku data users handbook. Japan Aerospace Exploration Agency.

Japan Aerospace Exploration Agency, 2012. GCOM-W/AMSR2 L3 Brightness Temperature (18Ghz) (1-Day,0.1 deg). https://doi.org/10.57746/EO.01gs73b1x2dj9eg42xamk1xnb1

Josberger, E.G., Mognard, N.M. (2002). A passive microwave snow depth algorithm with a proxy for snow metamorphism. Hydrol. Process. 16, 1557–1568. http: //dx.doi.org/10.1002/hyp.1020.

Karbou, F., Prigent, C., Eymard, L., & Pardo, J. R. (2005). Microwave land emissivity calculations using amsu measurements. IEEE Transactions on Geoscience and Remote Sensing, 43(5), 948–959. https://doi.org/10.1109/tgrs.2004.837503

Kerr, Y. H., Waldteufel, P., Wigneron, J.-P., Delwart, S., Cabot, F., Boutin, J., et al. (2010). The smos mission: New tool for monitoring key elements of the global water cycle. Proceedings of the IEEE, 98(5), 666–687. https://doi.org/10.1109/jproc.2010.2043032

Kilic, L., Prigent, C., Jimenez, C., Turner, E., Hocking, J., English, S., Meissner, T., Dinnat, E. (2023). Development of the surface fast emissivity model for ocean (SURFEM-ocean) based on the PARMIO radiative transfer model. Earth Space Sci. 10, http://dx.doi.org/10.1029/2022EA002785.

Kilic, L., Jimenez, C., Prigent, C., Korosov, A., Rampal, P., de Gelis, I., & Garric, G. (2025). Parameterization of the winter Arctic sea ice microwave emissivity between 1.4 and 36 GHz, for large scale applications. Earth and Space Science, 12, e2025EA004259. https://doi.org/10.1029/2025EA004259

Lawrence, H., Bormann, N., Sandu, I., Day, J., Farnan, J., Bauer, P. (2019). Use and impact of Arctic observations in the ECMWF numerical weather prediction system. Q. J. R. Meteorol. Soc. 145, 3432–3454. http://dx.doi.org/10.1002/qj.3628.

Lehner, B., Anand, M., Fluet-Chouinard, E., Tan, F., Aires, F., Allen, G. H., ... & Thieme, M. (2024). Mapping the world's inland surface waters: an update to the Global Lakes and Wetlands Database (GLWD v2). Earth System Science Data Discussions, 2024, 1-49.

Lindholm, A., Wahlström, N., Lindsten, F., Schön, T., 2022. Machine learning : a first course for engineers and scientists. Cambridge University Press.

Lindström, G., Pers, C., Rosberg, J., Strömqvist, J., Arheimer, B., 2010. Development and testing of the HYPE (Hydrological Predictions for the Environment) water quality model for different spatial scales. Hydrology Research 41, 295–319. https://doi.org/10.2166/nh.2010.007

MacKay, D.J., 1992. Bayesian interpolation. Neural Comput. 4, 415–447. http://dx.doi.org/10.1162/neco.1992.4.3.415.

Maeda, T., Taniguchi, Y., & Imaoka, K. (2016). Gcom-w1 amsr2 level 1r product: Dataset of brightness temperature modified using the antenna pattern matching technique. IEEE Transactions on Geoscience and Remote Sensing, 54(2), 770–782. https://doi.org/10.1109/tgrs.2015.

Masson, V., et al, The 765 SURFEXv7.2 land and ocean surface platform for coupled or offline simulation of earth surface variables and fluxes, Geoscientific Model Development, 6, 929–960, https://doi.org/https://doi.org/10.5194/gmd-6-929-2013, publisher: Copernicus GmbH, 2013.

Mätzler, C., Standley, A. (2000). Technical note: Relief effects for passive microwave remote sensing. Int. J. Remote Sens. 21, 2403–2412. http://dx.doi.org/10.1080/01431160050030538.

Meissner, T., Wentz, F., Manaster, A., Lindsley, R., Brewer, M., & Densberger, M. (2022). Remote sensing systems smap ocean surface salinities [level 3 running 8-day] [Dataset]. version 5.0 validated release. https://podaac.jpl.nasa.gov/dataset/SMAP_RSS_L3_SSS_SMI_8DAYRUNNINGMEAN_V3_70KM

Munchak, S. J., Ringerud, S., Brucker, L., You, Y., de Gelis, I., & Prigent, C. (2020). An active–passive microwave land surface database from gpm. IEEE Transactions on Geo-science and Remote Sensing, 58(9), 6224–6242. https://doi.org/10.1109/tgrs.2020.2975477

Napoly, A., et al., The interactions between soil–biosphere–atmosphere (ISBA) land surface model multi-energy balance (MEB) option in SURFEXv8 – Part 2: Introduction of a litter formulation and model evaluation for local-scale forest sites, Geoscientific Model Development, 10, 1621–1644, https://doi.org/10.5194/gmd-10-1621-2017, 2017.

Noilhan, J. and Mahfouf, J. F.: The ISBA land surface parameterisation scheme, Global and Planetary Change, 13, 145–159, https://doi.org/10.1016/0921-8181(95)00043-7, 1996.

Prigent, C., Rossow, W.B., Matthews, E. (1997). Microwave land surface emissivities estimated from SSM/I observations. J. Geophys. Res.: Atmospheres 102, 21867–21890. http://dx.doi.org/10.1029/97JD01360.

Prigent, C., Jimenez, C., & Bousquet, P. (2020). Satellite-derived global surface water extent and dynamics over the last 25 years (GIEMS-2). Journal of Geophysical Research: Atmospheres, 125(3), e2019JD030711.

Prigent, C., Jimenez, C., 2021. An evaluation of the synergy of satellite passive micro-wave observations between 1.4 and 36 GHz, for vegetation characterization over the tropics. Remote Sens. Environ. 257, 112346. http://dx.doi.org/10.1016/j.rse.2021.112346.

Rosenblatt, F. (1961). Principles of Neurodynamics. Perceptrons and the Theory of Brain Mechanisms. Technical Report, Cornell Aeronautical Lab Inc Buffalo NY.

Rosenfeld, S., Grody, N. (2000). Anomalous microwave spectra of snow cover observed from special sensor microwave/imager measurements. J. Geophys. Res.: At-mospheres 105, 14913–14925. http://dx.doi.org/10.1029/1999JD900486.

Rosenkranz, P. W. (2017). Line-by-line microwave radiative transfer (non-scattering). Technical Reports Series.

Santoro, M.; Cartus, O. (2023): ESA Biomass Climate Change Initiative (Biomass_cci): Global datasets of forest above-ground biomass for the years 2010, 2017, 2018, 2019 and 2020, v4. NERC EDS Centre for Environmental Data Analysis, 21 April 2023. doi:10.5285/af60720c1e404a9e9d2c145d2b2ead4e.

Sandells, M., Rutter, N., Wivell, K., Essery, R., Fox, S., Harlow, C., Picard, G., Roy, A., Royer, A., Toose, P. (2024). Simulation of Arctic snow microwave emission in surface-sensitive atmosphere channels. Cryosphere 18, 3971–3990. http://dx.doi.org/10.5194/tc-18-3971-2024.

Schyberg H., et al., Copernicus Climate Change Service: Arctic regional reanalysis on single levels from 1991 to present, https://doi.org/10.24381/CDS.713858F6, 2021.

Sturm, M., Benson, C.S. (1997). Vapor transport, grain growth and depth-hoar development in the subarctic snow. J. Glaciol. 43, 42–59. http://dx.doi.org/10.3189/S0022143000002793.

Uranga, E., Llorente, A., Gonzalez, J., de la Fuente, A., Oliva, R., Soldo, Y., & Jorge, F. (2022). Smos esa rfi monitoring and information tool: Lessons learned. Remote Sensing, 14(21), 5387. https://doi.org/10.3390/rs14215387

Weng, F., Yan, B., Grody, N.C. (2001). A microwave land emissivity model. J. Geophys. Res.: Atmospheres 106, 20115–20123. http://dx.doi.org/10.1029/2001JD900019.

Wiesmann, A., Mätzler, C. (1999). Microwave emission model of layered snowpacks. Remote Sens. Environ. 70, 307–316. http://dx.doi.org/10.1016/S0034-4257(99)00046-2

Yamashita, R., Nishio, M., Do, R.K.G. et al. Convolutional neural networks: an overview and application in radiology. Insights Imaging 9, 611–629 (2018). https://doi.org/10.1007/s13244-018-0639-9

Document History

Version	Author(s)	Date	Changes
0.01	Pete Weston	05/11/2025	Initial template
0.1	Iris de Gelis, Jostein Blyverket, Filipe Aires, Catherine Prigent, Asmund Bakketun, Cyril Palerme, Harald Schyberg	21/11/2025	First draft with comments/suggestions from Pete Weston
0.2	Iris de Gelis, Jostein Blyverket, Filipe Aires, Catherine Prigent, Asmund Bakketun, Cyril Palerme, Harald Schyberg, Ilaria Clemenzi, Jude Musuuza, David Gustafsson	27/11/2025	Draft for internal WP review
1.0	Iris de Gelis, Jostein Blyverket, Filipe Aires, Catherine Prigent, Asmund Bakketun, Cyril Palerme, Harald Schyberg, Ilaria Clemenzi, Jude Musuuza, David Gustafsson	10/12/2025	Updated and issued after internal reviews

Internal Review History

Internal Reviewers	Date	Comments
Kristina Froehlich (DWD) and Pete Weston (ECMWF)	Nov/ Dec 2025	Initial version